Computational Mechanics
https://doi.org/10.1007/s00466-024-02471-7

ORIGINAL PAPER

Modelling and simulation of anisotropic growth in brain tumours through poroelasticity: A study of ventricular compression and therapeutic protocols

Francesca Ballatore[1] · **Giulio Lucci**[2] · **Chiara Giverso**[1]

Received: 31 August 2023 / Accepted: 8 March 2024

Abstract
Malignant brain tumours represent a significant medical challenge due to their aggressive nature and unpredictable locations. The growth of a brain tumour can result in a mass effect, causing compression and displacement of the surrounding healthy brain tissue and possibly leading to severe neurological complications. In this paper, we propose a multiphase mechanical model for brain tumour growth that quantifies deformations and solid stresses caused by the expanding tumour mass and incorporates anisotropic growth influenced by brain fibres. We employ a sharp interface model to simulate localised, non-invasive solid brain tumours, which are those responsible for substantial mechanical impact on the surrounding healthy tissue. By using patient-specific imaging data, we create realistic three-dimensional brain geometries and accurately represent ventricular shapes, to evaluate how the growing mass may compress and deform the cerebral ventricles. Another relevant feature of our model is the ability to simulate therapeutic protocols, facilitating the evaluation of treatment efficacy and guiding the development of personalized therapies for individual patients. Overall, our model allows to make a step towards a deeper analysis of the complex interactions between brain tumours and their environment, with a particular focus on the impact of a growing cancer on healthy tissue, ventricular compression, and therapeutic treatment.

Keywords Brain tumours · Poroelasticity · Anisotropic growth · Ventricular compression · Therapeutic protocols · Finite element method

1 Introduction

Malignant brain tumours currently represent one of the most challenging medical problems. They can emerge in any region of the brain and are known for their aggressive nature, which makes them extremely difficult to treat [51]. Among the numerous issues caused by the growth of such cancers, the expansion of neoplastic tissue inevitably results in unnatural displacement of the normal cerebrum. As a consequence of this anomalous tissue motion within the skull fixed volume, the tumour can exert considerable pressure and solid stress onto the surrounding healthy tissue, leading to changes in neurological functionalities and in the flow of extracellular fluid. These side effects caused by a tumour growing within the brain are known as "mass effect" and can cause severe neurological dysfunctions, such as fatigue or drowsiness, alterations of consciousness, problems with vision, nausea and vomiting, headaches, epilepsy and seizures, changes in personality and other psychiatric disorders [5, 7, 118, 143, 155]. In general, the growth of a solid mass is associated with an increase in intracranial pressure, which in turn may provoke alterations in brain functions and cerebrospinal fluid flow obstruction. In particular, recent experiments and clinical evaluations underscored the relevant role played by solid stresses in addition to fluid pressure [142] and it was hypothesized that stresses in the tumour microenvironment may promote immune escape [130]. Moreover, pre-surgery tissue displacement due to mass effect may also be an indicator of the overall patient survival expectations [147]. Indeed, the development of unnatural strains and stresses due to tumour growth has been recognized as a relevant prognostic factor,

✉ Francesca Ballatore
francesca.ballatore@polito.it

[1] Department of Mathematical Sciences "G.L. Lagrange", Politecnico di Torino, Corso Duca degli Abruzzi 24, 10129 Turin, Italy

[2] Department of Structural and Geotechnical Engineering, Sapienza University of Rome, Via Eudossiana 18, 00184 Rome, Italy

Published online: 25 April 2024

with a negative impact on the patient, especially in the skull-confined brain [71, 98, 125, 147]. For all these reasons, it is important to evaluate brain alterations, displacements, and stresses caused by tumour growth also in distant parts of the tissue with respect to the tumour location [112]. Clinically, the degree of mass effect can be assessed through Magnetic Resonance Imaging (MRI) by quantifying the displacement of some relevant biological structures (e.g. the midline shift, the lateral ventricle displacement [112, 147] or the maximum displacement magnitude of the ventricles [175]), the compression of fluid-filled structures that may result in the obstruction of brain ventricles, and the formation of oedema in the region close to the tumour lesion [147]. In particular, an accurate estimation of ventricular compression caused by the neoplastic mass may also improve the computational reconstruction and segmentation of medical images, which is important to capture the correct tumour volume [97]. Furthermore, it is well recognized and evident from medical imaging that brain tumours exhibit anisotropic shapes and patterns, owing to preferential growth and cell migration along the directions of white matter tracts and blood vessels [33, 64, 74, 94, 100].

Regarding the therapeutic treatments, the current standard of care for brain tumours is the Stupp protocol [150, 151], which involves surgical resection of the mass followed by radiation therapy and adjuvant chemotherapy. Radiation therapy utilises high doses of radiation to target the tumour, shrink its size, and kill cancer cells. It is highly precise and can double the survival time compared with surgery alone [139]. The Stupp protocol also includes chemotherapy with temozolomide (TMZ), a cytotoxic agent that has been shown to significantly improve survival rates [134]. Nevertheless, there are cases in which gross resection of the mass is not feasible, mainly due to tumour location. This especially happens for patients with multifocal or eloquently located[1] glioblastomas [112] and for deeply infiltrating tumours in locations not amenable to surgery [114], which exhibit an unacceptable risk of post-operative neurological deficits. In these situations, appropriate chemoradiation therapies are even more relevant to reduce tumour burden and extend the survival time of patients while minimizing the side effects [25, 28, 112, 114]. However, the treatment and prognosis for brain tumours have only seen marginal improvement over the last decade due to the complexity of the tumour microenvironment and the limited ability of drugs to penetrate the blood-brain barrier [174]. Indeed, even with currently accepted care protocols, the median survival time does not exceed 15 months [151], and is even less in the absence of surgery [112, 150]. As a result, there is a pressing need for the development of novel and more effective therapeutic approaches to enhance outcomes for patients with brain cancer. Several different drugs, e.g. bevacizumab or irinotecan, as a substitute for or in combination with TMZ have recently been tested [104, 114], sometimes with limited success [43, 104]. In this respect, the contribution of mathematical models can be helpful to perform realistic, personalised simulations with the aim of evaluating *in silico* the potential efficacy of therapeutic protocols before administering them to patients.

In particular, during the last decade, various mathematical models have been developed to understand the progression of brain tumours, with the aim of supporting clinical observations. The models used to study glioma growth at the microscale are mainly Agent-Based Models, like Cellular Automata or Cellular Potts Models [34, 82, 99, 101, 119], which are suitable to describe tumour early growth, as well as invasion-metastasis of small groups of cells and phenotypic plasticity. On the other hand, macroscopic models describe the evolution of cancer at the tissue scale through continuous variables, whereas mesoscopic and multiscale models [48, 49, 62, 63, 132, 158] are used in several works to bridge the gap between scales. Seminal studies employing reaction-diffusion equations [159–162, 166, 173] to model the spreading and proliferation of gliomas laid the foundations for numerous successive investigations, with an increasing level of detail and focusing on different aspects, like intra-tumoural and tissue heterogeneity, anisotropy, invasiveness, and immune interaction [2, 4, 47, 91, 94, 102, 156]. Biomechanical models, instead, also account for the mechanically induced alterations onto the surrounding tissue by the growing mass and vice versa [18, 19, 23, 33, 35, 45, 58–60, 86, 109, 116, 154], which are important issues. For a more detailed classification of mathematical models developed for brain tumour growth, we refer the reader to [9, 23]. What is worth noting here is that the vast majority of mechanical models do not include anisotropic growth distortions. The latter are related to tumours growing preferentially along the white matter tracts and displacing the host tissue accordingly. Even though the mechanical framework proposed in [23, 116] is able to evaluate the stress and strain fields associated with brain cancer expansion, it does not include the modelling of anisotropic distortions specifically related to growth. An attempt in this respect has been made in a recent work by Harkos et al. [81], where three different evolution equations for the growth stretches in the principal directions were introduced. However, such equations were based on a purely phenomenological exponential law, to preferentially drive growth along the direction of reduced compression [81, 117]. Another important issue that is generally overlooked in mechanical models of brain tumour growth is the description of therapeutic protocols. Previous mathematical studies about therapies for brain cancer can be found in [2, 24, 32, 48, 87, 92, 93, 111, 134, 138–140], which however are grounded

[1] In the jargon of neurosurgery, eloquent brain areas are defined as zones whose neurological function is clearly identified and hence, if injured, may lead to disabilities [84, 103].

on ordinary differential equations and kinetic equations, not discussing the interplay with mechanics. Recent investigations by Hormuth et al. [89, 91] considered the effect of Von Mises stress in a model for brain tumour growth and response to chemoradiation. Notably, the stress was used to exponentially dampen the motility coefficient of tumour cells, while the mechanical constitutive equations remained relatively simplified, and fluid stresses were not considered.

On the basis of these observations, in this paper we propose a multiphase mechanical model for brain tumour growth which is able to quantify anisotropic deformations, solid and fluid stresses induced by the growing mass and to embed therapeutic protocols. Additionally, a novelty of our work is the study of cerebral ventricles compression, caused by brain tumour growth, and alterations in their shape due to the cancer-induced deformation. Our model extends the one proposed in [116] by clearly separating the tumour from the host tissue with a sharp interface that moves with the solid phase, resulting in variables that are not necessarily continuous across such an interface. Moreover, a key feature of our model is the inclusion of an anisotropic growth tensor that accounts for the directions of brain fibres reconstructed from medical imaging data. In this respect, our approach generalizes the biomechanical ones based on isotropic growth [18, 19, 23, 58, 116] and also differs from the one by Harkos et al. [81], where the influence of patient-specific parameters on the anisotropic growth tensor was indirect. Indeed, in [81] the evolution laws for the growth stretch rates in the three directions were driven by the stresses, which were affected by, but not directly reconstructed from, Magnetic Resonance Elastography data. Furthermore, the model we propose also includes image-based diffusion and permeability tensors, the latter of which is not considered in [81]. These choices allow to reproduce the irregular and heterogeneous growth patterns of brain tumours, which are influenced by the surrounding anatomical structures [64, 167]. In particular, to construct a realistic three-dimensional brain geometry and establish the ventricles' shape, we used patient-specific Magnetic Resonance Imaging (MRI) data. Specifically, we took advantage of data collected by Diffusion Tensor Imaging (DTI), an MRI technique that captures anisotropic water diffusion and estimates the axonal white matter organization in the brain. These data were processed with an approach based on a multi-compartment model to isolate the free water contribution and to give more weight to water motion constrained by brain fibres. Additionally, we used the mechanical variables provided by our model to modify the DTI-acquired data as the tumour grows and alters the host tissue. By considering the interactions between the tumour expansion and the surrounding brain environment deformation, our model makes a step towards a more complete understanding of the complex processes underlying brain tumour growth and the resulting pathological effects. The proposed framework also incorporates a simple model to simulate therapeutic protocols, which is a relevant feature towards the development of improved treatments for patients. Differently from recent works that introduced mechanical effects into chemoradiation models for brain tumours [89–91], our framework accounts for nonlinear elasticity of both the tumour and the host tissue, with constitutive equations motivated by experimental data [22], and incorporates both solid and fluid stresses. Furthermore, the coupling between mechanics and growth is derived via well-established Continuum Mechanics methods in a physically motivated way. Although the stress feedback on tumour growth is not considered here, it can be straightforwardly incorporated, as done in [116].

In detail, the remainder of this work is organised as follows. In Sect. 2, we outline the mathematical model and the procedures to reconstruct its patient-specific anisotropic components. Then, in Sect. 3 we describe the numerical implementation and provide an estimate of the parameters involved. Section 4 is devoted to the presentation and discussion of the main results concerning numerical simulations of the model. Finally, we conclude with Sect. 5, in which we summarise the main aspects of the work and we discuss some possible perspectives for future research.

2 Mathematical model for brain tumour growth

In this Section, we present a mathematical model grounded on Continuum Mechanics and poroelasticity to describe brain tumour growth, proliferation, and treatment. Specifically, the mass and momentum balances, along with the constitutive assumptions, are presented in Sect. 2.1. The anisotropic description of diffusion, permeability, and growth tensors, along with their evolution over time, is discussed in Sect. 2.2. Finally, the interface, boundary, and initial conditions required to solve the model equations are provided in Sect. 2.3.

2.1 Model derivation

We model the brain as a continuum multiphase body whose reference configuration is identified by a region Ω^* in the three-dimensional Euclidean space $\mathcal{E}$. Within this referential domain, we consider the sub-region occupied by the tumour, denoted by Ω_t^*, which is completely separated from the sub-region representing the healthy host tissue, denoted by Ω_h^*. Hence, the boundary $\partial\Omega_t^*$ between the tumour and the surrounding environment can be described by a sharp interface. This is appropriate to represent localised, non-invasive brain tumours, which do not infiltrate much in the host tissue and have significantly different biomechanical properties from it. Such tumours are indeed the ones associated with the high-

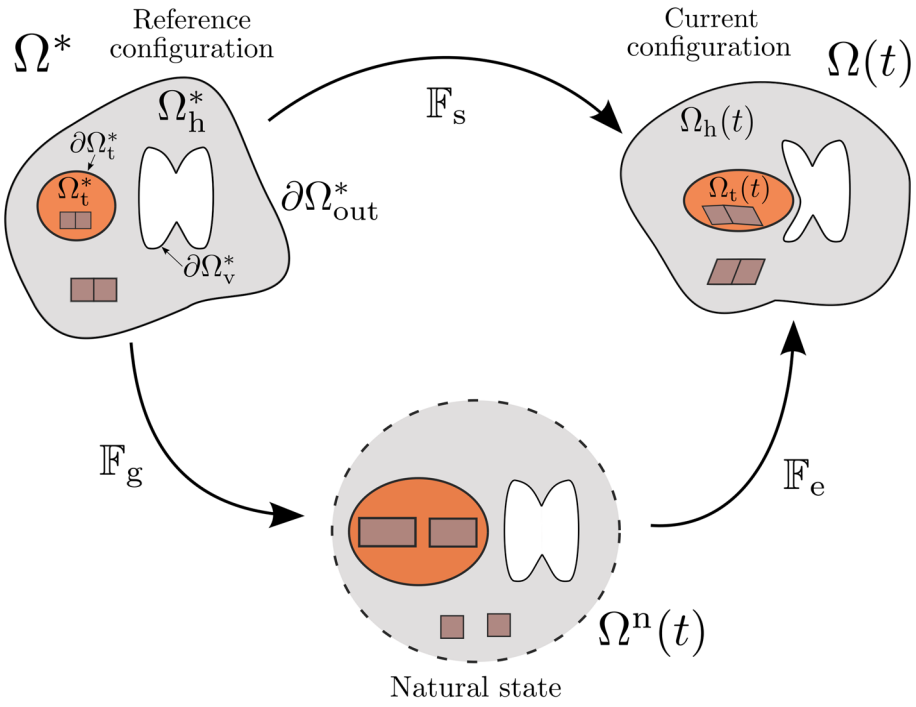

Fig. 1 Sketch of the domains involved in the model and of the multiplicative decomposition of the deformation gradient. (Color figure online)

est mass effect [45, 116, 127, 147]. Moreover, we assume that the cerebral ventricles can be represented by a hole in the domain. Therefore, the boundary of the brain domain is $\partial\Omega^* = \partial\Omega^*_{out} \cup \partial\Omega^*_v$, where $\partial\Omega^*_{out}$ stands for the outer boundary, which can be interpreted as the skull, and $\partial\Omega^*_v$ represents instead the boundary of the ventricular region (see Fig. 1 for a schematic representation). As a result, in order to properly study the impact of cancer growth on the ventricles without describing the complex mechanisms that can occur inside them, appropriate boundary conditions have to be imposed on $\partial\Omega^*_v$, as we will discuss in Sect. 2.3.

Working in the framework of poroelasticity, both the healthy region Ω^*_h and the diseased one Ω^*_t are treated as saturated domains, composed of two distinct phases: the solid phase, labelled with subscript "s", representing the cellular components of the brain tissue, and the liquid phase, labelled with subscript "ℓ". Therefore, introducing the volumetric fraction of the cell population, ϕ_s, and the volumetric fraction of the liquid, ϕ_ℓ, the saturation constraint

$$\phi_s + \phi_\ell = 1 \tag{1}$$

must hold at any time instant and at any point in the brain domain $\Omega^* = \Omega^*_h \cup \Omega^*_t$. In this description, the cellular phase represents healthy cells in Ω^*_h and diseased cells in Ω^*_t, whereas the fluid phase resumes interstitial brain fluid, blood and nutrients in both regions. Furthermore, we assume that the materials composing the phases are incompressible, which means that both phases of the mixture have constant true densities $\hat{\rho}_\alpha$, with $\alpha \in \{s, \ell\}$. For this reason, once the true density $\hat{\rho}_\alpha$ is prescribed, the apparent phase density $\rho_\alpha := \hat{\rho}_\alpha \phi_\alpha$ of the material composing the α-phase is totally defined by knowing ϕ_α. Finally, since cells are mainly composed of water, we assume that the true densities of both phases are equal to each other, i.e. $\hat{\rho}_s = \hat{\rho}_\ell$.

Concerning the kinematics, let $\chi(\mathbf{X}, t)$ be the motion of the body, which maps a material point $\mathbf{X} \in \Omega^*$ to its current position $\mathbf{x} \in \Omega$ at time t. The displacement field of the solid phase is, then, defined by $\mathbf{u}_s(\mathbf{X}, t) = \chi(\mathbf{X}, t) - \mathbf{X}$, so that the *deformation gradient tensor* of the solid component is $\mathbb{F}_s = \mathbb{I} + \mathrm{Grad}\,\mathbf{u}_s$, where $\mathbb{I}$ is the second order identity tensor and Grad denotes the gradient with respect to material coordinates. In order to properly describe the mechanics of the growing tumour, we have to face the problem that the environment is constantly changing as cells duplicate and die, and it is not trivial to define a reference configuration with respect to which deformations are measured. Therefore, we resort to the theory of *evolving natural configurations*, proposed in [55, 115, 136] and successfully applied to model growth and remodelling of living tissues in different contexts [11–15, 19, 77, 79, 116, 120]. Following this modelling background, we adopt a multiplicative decomposition of the deformation gradient of the solid phase:

$$\mathbb{F}_s = \mathbb{F}_e \mathbb{F}_g\,. \tag{2}$$

Such a decomposition, represented pictorially in Fig. 1, accounts for the fact that the variation of mass due to growth induces inelastic distortions in the body, which in turn generate residual stresses. This is translated in mathematical terms

by considering a *growth tensor* $\mathbb{F}_g$, which describes the local change of shape and volume caused by growth, whereas $\mathbb{F}_e$ represents the purely elastic part of the deformation. The tensor $\mathbb{F}_g$ determines the so-called *natural state* $\Omega^n(t)$ of the body, in which each material particle is allowed to grow freely and independently of the other ones, while the elastic accommodation within the material is described by $\mathbb{F}_e$.

Furthermore, since the deformation gradient $\mathbb{F}_s$ is invertible, from Eq. (2) it follows that $\mathbb{F}_e$ and $\mathbb{F}_g$ are non-singular as well. Indeed, the determinant J_s of the deformation gradient can be expressed as $J_s = J_e J_g$, where $J_e := \det \mathbb{F}_e$ and $J_g := \det \mathbb{F}_g$.

2.1.1 Mass balance laws and definition of the therapeutic protocol

The multiphase approach employed to describe tumour growth is based on the theory of mixtures [13, 16, 40, 137]. Specifically, the Lagrangian formulation of the mass balance equations for the solid and liquid phases in the tumour reference domain Ω_t^* can be written, respectively, as [23, 79, 116]:

$$\dot{\overline{J_s \phi_s}} = J_s \Gamma_s(\phi_s, c_n, t)\,, \tag{3}$$

$$\dot{\overline{J_s \phi_\ell}} + \mathrm{Div}\left[J_s \phi_\ell \mathbb{F}_s^{-1}\,(\mathbf{v}_\ell - \mathbf{v}_s)\right] = -J_s \Gamma_s(\phi_s, c_n, t)\,, \tag{4}$$

where the differential operator Div denotes the divergence with respect to the material point in the reference configuration, $\mathbf{v}_s$ and $\mathbf{v}_\ell$ are the velocities of the solid and fluid constituents, respectively, and a superposed dot denotes the time derivative. Instead, Γ_s represents the net mass growth rate of the solid phase and it is assumed to be a function of the cell volume fraction ϕ_s and of the concentration of available nutrients c_n, the latter normalised with respect to the physiological value. In particular, the evolution in time and space of c_n can be written in Lagrangian form as follows [23, 116]:

$$J_s \phi_\ell \dot{c}_n - \frac{\mathbb{K}^*}{\mu}\,\mathrm{Grad}\, p \cdot \mathrm{Grad}\, c_n - \mathrm{Div}\left[\phi_\ell \mathbb{D}^*\,\mathrm{Grad}\, c_n\right] = J_s G_n\,, \tag{5}$$

where p is the fluid pressure, $\mathbb{D}^* := J_s \mathbb{F}_s^{-1} \mathbb{D} \mathbb{F}_s^{-\mathrm{T}}$ is the pullback of the diffusion tensor $\mathbb{D}$ and $\mathbb{K}^* := J_s \mathbb{F}_s^{-1} \mathbb{K} \mathbb{F}_s^{-\mathrm{T}}$ is the pullback of the permeability tensor $\mathbb{K}$, whose construction will be discussed extensively in Sect. 2.2. Instead, G_n is taken as:

$$G_n = \begin{cases} -\zeta \phi_s \phi_\ell c_n + S_n\,(1 - c_n)\,\phi_\ell & \text{in } \Omega_t^* \\ 0 & \text{in } \Omega_h^* \end{cases}, \tag{6}$$

so that nutrients are consumed by the tumour at a constant rate ζ and supplied at a constant rate S_n if their concentration is below the physiological one. In particular, we hypothesize that a net nutrients uptake only happens within the tumour region, where a net growth is occurring. We remark that Eqs. (3)–(4) have been derived, as in standard mixture theory, with respect to the motion of the solid phase, for both constituents. Thus, the tumour region Ω_t^* in the reference configuration does not evolve in time. Furthermore, in writing Eqs. (3)–(4), we have assumed that growth of the solid phase happens at the expense of the liquid phase. This assumption stands from the biological observation that cells need to absorb fluid from the extracellular environment in order to increase their volume and proliferate. At the same time, when cells die, in the absence of calcification, they release the intracellular fluid into the environment. However, a tissue is generally not a closed system in terms of mass since fluid can come from the vasculature within the tissue or from the boundary between the tissue and fluid regions, such as the brain ventricles. In the present description, as largely done in the literature [3, 40, 47, 122], we neglect the description of the extra fluid coming from the vasculature, but fluid can eventually flow across the boundary between the tissue and the liquid region of the brain ventricles, therefore, the total mass of the mixture is not conserved. More in detail, we assume the following form for the net rate of growth Γ_s:

$$\Gamma_s(\phi_s, c_n, t) = \begin{cases} \nu \phi_s\,(\phi_{\max} - \phi_s)\,(c_n - c_0)_+ - R(\phi_s, t) - G(\phi_s, t) & \text{in } \Omega_t^* \\ 0 & \text{in } \Omega_h^* \end{cases}, \tag{7}$$

where $(\cdot)_+$ denotes the positive part of its argument and $\nu > 0$. Specifically, in the domain occupied by the host tissue Ω_h^*, we assume that proliferation of healthy cells is compensated by their natural death, so that the net rate of growth Γ_s can be taken as equal to zero therein. Conversely, the first term on the right-hand side of Eq. (7) in Ω_t^* models contact inhibition of proliferation above a maximum cell volume fraction $\phi_{\max}$ as well as the dependence of proliferation on the concentration of nutrients c_n, with an hypoxia threshold c_0 [23, 47, 116]. For what concerns the loss terms $R(\phi_s, t)$ and $G(\phi_s, t)$, they represent cell death due to radiotherapy and chemotherapy, respectively. We define them by referring to the current standard of care for newly diagnosed brain tumours, which consists of adjuvant radiotherapy (RT) and chemotherapy (CHT), very often after surgical resection. In some cases, however, resection of the tumour mass is unfeasible, and only RT and CHT are administered. A protocol about the administration of the drug temozolomide combined with radiotherapy treatment for brain tumours was proposed by Roger Stupp in 2005 [151]. In particular, he found that the addition of TMZ to radiotherapy for newly diagnosed glioblastoma resulted in a clinically meaningful and statistically significant survival benefit with minimal additional

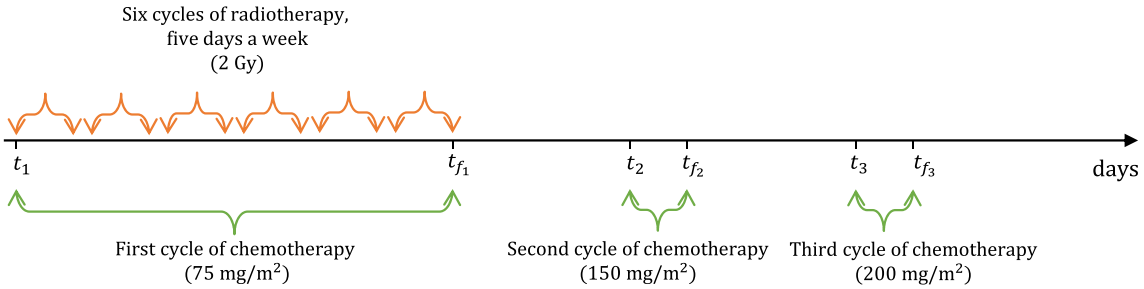

Fig. 2 The therapeutic protocol considered in this work: radiotherapy (in orange) and three cycles of chemotherapy (in green). (Color figure online)

toxicity for the patient. The radiotherapy administration of the Stupp protocol consists of fractionated focal irradiation at a dose of 2 Gy per fraction (1 Gy = 1 J/kg), given once a day five days per week (Monday through Friday) over a period of six weeks, for a total dose of 60 Gy. Concomitant chemotherapy consists of TMZ at a dose of 75 mg/m^2, to be administered 7 days per week starting from the first day of radiotherapy until the last day of radiotherapy. After a 4-week break, patients receive up to six additional cycles of chemotherapy according to the standard 5-day schedule every 28 days. The standard dose of TMZ in the second adjuvant CHT cycle is 150 mg/m^2 and it is increased to 200 mg/m^2 beginning with the third cycle.

The effects of radiotherapy and chemotherapy according to a therapeutic protocol similar to the standard Stupp protocol, with just three cycles of chemotherapy, as illustrated in Fig. 2, are introduced in our model by taking $R(\phi_s, t)$ and $G(\phi_s, t)$ as directly proportional to the fraction of tumour cells [2, 48, 134, 139]:

$$R(\phi_s, t) = k_R(t)\phi_s\,, \qquad G(\phi_s, t) = k_C(t)\phi_s\,. \tag{8}$$

Following other works in the literature [2, 48, 134], we firstly investigate the case in which the two time-dependent coefficients $k_R(t)$ and $k_C(t)$ are equal to zero when the therapy is not administered, while they are constant and equal to the specific cell death rate during the days of treatment, i.e.,

$$k_R(t) = \begin{cases} R_{\text{eff}} & t_1 + 7j \text{ days} \le t \le t_1 + (4 + 7j) \text{ days} \\ 0 & \text{otherwise} \end{cases}, \tag{9a}$$

$$k_C(t) = \begin{cases} k_{C1} & t_1 \le t \le t_{f1} \\ k_{C2} & t_2 \le t \le t_{f2} \\ k_{C3} & t_3 \le t \le t_{f3} \\ 0 & \text{otherwise} \end{cases}, \tag{9b}$$

where $j = 0, \ldots, 5$, t_1 is the time when the patient starts therapies, t_2 and t_3 are the days when the patient starts the second and the third cycle of chemotherapy (i.e., in our case, $t_2 = t_1 + 70$ days and $t_3 = t_1 + 105$ days) and t_{f_i} are the days in which each chemotherapeutic cycle ends (i.e. $t_{f_1} = t_1 + 39$ days, $t_{f_2} = t_1 + 74$ days and $t_{f_3} = t_1 + 109$ days). For what concerns radiotherapy, the term R_{eff} represents the effect of n fractions per day and it is estimated through the linear-quadratic model, commonly used for studying the survival response and clinical results in radiotherapy [2, 134, 171]:

$$R_{\text{eff}} = \alpha n d + \beta n d^2\,, \tag{10}$$

where d [Gy] is the dose radiation for every fraction, while α [Gy^{-1}] and β [Gy^{-2}] are the linear and quadratic coefficients for RT-induced cell death, respectively. For what concerns chemotherapy, the parameters k_{C1}, k_{C2} and k_{C3} appearing in Eq. (9b) reflect the cell death response for increasing drug dosage, as described above. Then, we investigate another modelling assumption to take into account the fact that the effects of drug administration persist even after the drug has been cleared out from the body, since complex biological processes are triggered [68]. Indeed, late apoptosis/necrosis induced by TMZ may occur even after some days from the last treatment [30, 83, 141]. To account for this prolonged effect of chemotherapy on tumour cells without resorting to a complex pharmacodynamics model, we consider an exponential decay of the tumour cell response (in terms of the cell death rate k_C) when each chemotherapy cycle is stopped. As a consequence, the coefficient $k_C(t)$ in Eq. (8) in this case is not null when the chemotherapy is not administered, but instead it decays in time as follows:

$$k_C(t) = \sum_{i=1}^{3} k_{Ci}\,\mathbb{1}_{[t_i, t_{fi}]}(t) + k_{Ci}\,e^{-\lambda_c (t - t_{fi})}\,\mathbb{1}_{[t_{fi}, +\infty)}(t)\,, \tag{11}$$

where $\mathbb{1}_{[a,b]}(t)$ is the indicator function whose value is one for $a \le t \le b$ and is equal to zero otherwise. More details on the values of the parameters k_{Ci} are given in Sect. 3.2 together

with the plot of the time evolution of $k_R(t)$ and $k_C(t)$ for all the considered scenarios (see Fig. 9).

2.1.2 Momentum balance laws

Regarding the momentum balances in both the cancer and healthy domains, for the fluid phase we assume the validity of Darcy's law [23, 76]:

$$\mathbf{v}_\ell - \mathbf{v}_\mathrm{s} = -\mathbb{F}_\mathrm{s}\frac{\mathbb{K}^*}{J_\mathrm{s}\mu\phi_\ell}\,\mathrm{Grad}\,p\,, \tag{12}$$

in which p is the pressure of the interstitial fluid and $\mathbb{K}^* = J_\mathrm{s}\mathbb{F}_\mathrm{s}^{-1}\mathbb{K}\mathbb{F}^{-\mathrm{T}}$ is the tensor pullback to the reference configuration of the permeability tensor $\mathbb{K}$ in the current configuration, that will be discussed in Sect. 2.2. Instead, the balance of linear momentum for the mixture as a whole reads

$$\mathrm{Div}\left[-J_\mathrm{s}p\mathbb{F}_\mathrm{s}^{-\mathrm{T}} + \mathbb{P}_\mathrm{s}\right] = \mathbf{0}\,, \tag{13}$$

where $\mathbb{P}_\mathrm{s}$ is the constitutively determined part of the first Piola-Kirchhoff stress tensor of the solid phase, that will be derived in Sect. 2.1.3. For later convenience, it is useful to reformulate the mass balances by summing up Eqs. (3) and (4) and using Eqs. (1) and (12), to obtain

$$\dot{J}_\mathrm{s} = \mathrm{Div}\left[\frac{\mathbb{K}^*}{\mu}\,\mathrm{Grad}\,p\right]. \tag{14}$$

For further details about the derivation of Eqs. (12)–(14) we refer the reader to [23].

2.1.3 Stress tensor and constitutive equations

In order to close the system of mass and momentum balance equations and to understand how brain tumour growth influences mechanically the surrounding tissues, we have to provide a constitutive equation for $\mathbb{P}_\mathrm{s}$, i.e., the effective part of the first Piola-Kirchhoff stress tensor associated with the cellular population, both in the diseased and in the healthy region. In analogy with [14, 116], we assume that the mechanical response is hyperelastic from the natural state to the current configuration, so the tumour is modelled as a hyperelastic material capable of growing. Therefore, we assume the existence of an elastic strain energy density function for both the tumour and the healthy tissue, from which we compute the corresponding stress $\mathbb{P}_\mathrm{s}$.

Specifically, in order to describe the mechanical behaviour of soft brain tissue, the generalised Ogden model [129] is often found appropriate [123]. We consider here the Mooney-Rivlin model, which represents a particular case of the generalised Ogden energy [22, 52, 123], and assume the brain to be mechanically isotropic, as pointed out experimentally [38, 56]. Hence, let $\overline{\mathbb{C}}_\mathrm{e} := J_\mathrm{e}^{-2/3}\mathbb{C}_\mathrm{e}$ be the isochoric part of the elastic right Cauchy-Green deformation tensor $\mathbb{C}_\mathrm{e} := \mathbb{F}_\mathrm{e}^{\mathrm{T}}\mathbb{F}_\mathrm{e}$. The strain energy density per unit volume of the natural state of the tumour, $\widehat{\mathcal{W}}_\mathrm{sn}^\mathrm{t}$, and of the healthy tissue, $\widehat{\mathcal{W}}_\mathrm{sn}^\mathrm{h}$, can be expressed as

$$\widehat{\mathcal{W}}_\mathrm{sn}^\omega\left(\overline{\mathbb{C}}_\mathrm{e}, J_\mathrm{e}\right) = \frac{1}{2}\mu_{1\omega}\left(\mathrm{I}_{\overline{\mathbb{C}}_\mathrm{e}} - 3\right) + \frac{1}{2}\mu_{2\omega}\left(\mathrm{II}_{\overline{\mathbb{C}}_\mathrm{e}} - 3\right) + \\ + \kappa_\omega\left(1-\phi_\mathrm{sn}\right)^2\left(\frac{J_\mathrm{e}-1}{1-\phi_\mathrm{sn}} - \ln\frac{J_\mathrm{e}-\phi_\mathrm{sn}}{1-\phi_\mathrm{sn}}\right), \tag{15}$$

where $\mathrm{I}_{\overline{\mathbb{C}}_\mathrm{e}} := \mathrm{tr}\left(\overline{\mathbb{C}}_\mathrm{e}\right)$, $\mathrm{II}_{\overline{\mathbb{C}}_\mathrm{e}} := \frac{1}{2}\left[\left(\mathrm{tr}\,\overline{\mathbb{C}}_\mathrm{e}\right)^2 - \mathrm{tr}\left(\overline{\mathbb{C}}_\mathrm{e}^2\right)\right]$, $\phi_\mathrm{sn} := J_\mathrm{e}\phi_\mathrm{s}$ is the volume fraction of the solid phase computed in the natural state, and $\mu_{1\omega}, \mu_{2\omega}, \kappa_\omega$ are material constitutive parameters of the ω-tissue, with $\omega \in \{\mathrm{t}, \mathrm{h}\}$ representing the tumour and the healthy region, respectively. The last term on the right-hand side of Eq. (15) penalises volumetric changes in the solid phase, occurring below the compaction point, i.e. when all pores in the medium are closed and further volume deformations are impeded due to the incompressibility of the solid constituent (see [57] for further details). Such a response to volumetric deformations is weighted by the material parameter κ_ω.

Then, given the strain energy density $\widehat{\mathcal{W}}_\mathrm{sn}^\omega$, we can express the first Piola-Kirchhoff stress tensor of the cellular phase in the ω-tissue, with $\omega \in \{\mathrm{t}, \mathrm{h}\}$, as

$$\mathbb{P}_\mathrm{s}^\omega = 2J_\mathrm{g}\mathbb{F}_\mathrm{e}\frac{\partial\widehat{\mathcal{W}}_\mathrm{sn}^\omega}{\partial\mathbb{C}_\mathrm{e}}\mathbb{F}_\mathrm{g}^{-\mathrm{T}}. \tag{16}$$

By working out the derivative in Eq. (16), we have

$$\mathbb{P}_\mathrm{s}^\omega = 2J_\mathrm{g}\mathbb{F}_\mathrm{e}\left[J_\mathrm{e}^{-2/3}\left(\underline{\underline{\mathbb{I}}} - \frac{1}{3}\overline{\mathbb{C}}_\mathrm{e}^{-1}\otimes\overline{\mathbb{C}}_\mathrm{e}\right) : \left(\gamma_1^\omega\,\mathbb{I} + \gamma_2^\omega\,\overline{\mathbb{C}}_\mathrm{e}\right)\right]\mathbb{F}_\mathrm{g}^{-\mathrm{T}} + \\ + \kappa_\omega\left(1-\phi_\mathrm{sn}\right)J_\mathrm{s}\left(1 - \frac{1-\phi_\mathrm{sn}}{J_\mathrm{e}-\phi_\mathrm{sn}}\right)\mathbb{F}_\mathrm{s}^{-\mathrm{T}}, \tag{17}$$

being $\underline{\underline{\mathbb{I}}}$ the symmetric fourth-order identity tensor and defining the quantities $\gamma_1^\omega := \frac{1}{2}\mu_{1\omega} + \frac{1}{2}\mathrm{I}_{\overline{\mathbb{C}}_\mathrm{e}}\mu_{2\omega}$ and $\gamma_2^\omega := -\frac{1}{2}\mu_{2\omega}$, for $\omega \in \{\mathrm{t}, \mathrm{h}\}$.

Finally, since we are considering a growth phenomenon, we also need to provide a constitutive equation which describes the evolution of the growth tensor $\mathbb{F}_\mathrm{g}$ in the tumour region. Indeed, since the net source term Γ_s is null in the healthy tissue (see Eq. (7)), the multiplicative decomposition of the deformation gradient is in principle not needed within the domain Ω_h^*, where no growth occurs. For this reason, coherently with our modelling approach, we take $\mathbb{F}_\mathrm{g} = \mathbb{I}$ inside Ω_h^* at all times.

Regarding the growth evolution in the tumour region, by substituting the product $J_s = J_e J_g$ into Eq. (3), the mass balance law of the solid phase takes the form:

$$J_g \dot{\overline{J_e \phi_s}} + \dot{J}_g J_e \phi_s = J_s \Gamma_s(\phi_s, c_n, t) \,. \tag{18}$$

Recalling that $\phi_{sn} = J_e \phi_s$ and defining the strain rate tensor $\mathbb{L}_g := \dot{\mathbb{F}}_g \mathbb{F}_g^{-1}$ (or velocity gradient) related to $\mathbb{F}_g$, we take advantage of the identity $\dot{J}_g = J_g \,\mathrm{tr}\left(\mathbb{L}_g\right)$ to rewrite Eq. (18) as

$$J_g \dot{\phi}_{sn} + J_g \,\mathrm{tr}\left(\mathbb{L}_g\right) \phi_{sn} = J_s \Gamma_s(\phi_s, c_n, t) \,. \tag{19}$$

Finally, we enforce the natural condition that the variation of body mass is given by the strain rate tensor associated with growth [12, 16, 76, 120], so that the following relation has to hold:

$$\mathrm{tr}\left(\mathbb{L}_g\right) = \frac{\Gamma_s}{\phi_s} \,. \tag{20}$$

This assumption also entails that the solid volumetric fraction in the natural state ϕ_{sn} is constant in time [16, 120]. Then, we can rewrite Eq. (3) as

$$J_s \phi_s = J_g \phi_{sn} \,, \tag{21}$$

stating that ϕ_s is fully determined once J_s and J_g are known. For what concerns the inelastic distortions related to growth, several models in the literature consider $\mathbb{F}_g$ as isotropic (see for instance [12, 15, 16, 18, 23, 76, 116, 120]). In this paper, differently from previous mechanical models for brain tumour growth [18, 23, 116], we consider instead an anisotropic growth tensor. Indeed, clinical evidence showed that brain cancers often grow following the white matter tracts [33, 64, 74, 94, 100], which preferentially drive tumour expansion along certain directions. To include such an effect in our model, we will consider a general anisotropic growth tensor in the form

$$\mathbb{F}_g = g_1 \mathbf{w}_1 \otimes \mathbf{w}_1 + g_2 \mathbf{w}_2 \otimes \mathbf{w}_2 + g_3 \mathbf{w}_3 \otimes \mathbf{w}_3 \,, \tag{22}$$

where $\mathbf{w}_i$, $i = 1, 2, 3$, are the unit orthogonal eigenvectors representing the principal directions of growth and g_i, $i = 1, 2, 3$, are the corresponding eigenvalues. Since the eigenvectors $\mathbf{w}_i$, with $i = 1, 2, 3$, are assumed to be time-independent, from Eq. (20) it follows that the three distinct eigenvalues of $\mathbb{F}_g$ must satisfy

$$\frac{\dot{g}_1}{g_1} + \frac{\dot{g}_2}{g_2} + \frac{\dot{g}_3}{g_3} = \frac{\Gamma_s}{\phi_s} \,. \tag{23}$$

This condition is for instance fulfilled if the evolution laws of the eigenvalues g_i are written as:

$$\frac{\dot{g}_1}{g_1} = \beta_1 \frac{\Gamma_s}{\phi_s} \,, \qquad \frac{\dot{g}_2}{g_2} = \beta_2 \frac{\Gamma_s}{\phi_s} \,, \qquad \frac{\dot{g}_3}{g_3} = \beta_3 \frac{\Gamma_s}{\phi_s} \,, \tag{24}$$

where β_i, $i = 1, 2, 3$, are proper coefficients that weigh growth along the principal directions and such that $\beta_1 + \beta_2 + \beta_3 = 1$. The choice of the coefficients β_i and the eigenvectors $\mathbf{w}_i$ will be discussed properly in Sect. 2.2, referring to medical patient-specific data.

2.2 Anisotropic diffusion, permeability, and growth

The presence of white matter tracts within the brain introduces directional anisotropy that clearly affects all the relevant phenomena, including diffusion, fluid motion, and tumour growth. To properly account for the role of preferential directions, it is therefore necessary to provide definitions for the diffusion tensor $\mathbb{D}$, the permeability tensor $\mathbb{K}$, and the growth tensor $\mathbb{F}_g$ which reflect the *in vivo* anisotropy. In addition, the expansion of the tumour mass displaces the fibres in the surrounding environment, leading to a modification of the directions of anisotropy in the current configuration $\Omega(t)$. Thus, we use the mechanical description included in our model to progressively modify the tensors as time evolves.

To model anisotropic phenomena, we start from a set of patient-specific data collected through Magnetic Resonance Imaging (MRI), and, in particular, Diffusion Tensor Imaging (DTI), provided by Istituto Neurologico Carlo Besta in Milan (Italy). This procedure allows to reconstruct a realistic brain geometry and environment, with the aim of providing a framework potentially capable of embedding patient-specific information. In detail, the main advantages of MRI lie in its efficiency in detecting brain tumours and its capability to highlight the different types of tissue composing the brain. Furthermore, it enables us to clearly identify the ventricle cavities, which are important for our study. Moreover, DTI is an MRI technique for characterising the micro-structural architecture of the brain components and for deriving the preferential directions of water diffusion inside the tissue. The capacity of DTI to determine the anisotropic diffusion of water molecules provides the means to identify and visualise the white matter neural tracts and, consequently, the preferential directions of nutrients diffusion, cell migration, and growth. The reconstruction of the boundaries of the brain and the ventricles, as well as the processing of DTI data, are summarized in Appendix B. We then take advantage of the DTI images to extrapolate the relevant information on the diffusion, permeability, and growth tensors, as discussed in the following.

Diffusion tensor $\mathbb{D}$. The diffusion tensor at the initial time instant $\mathbb{D}^0$ is reconstructed by using data from DTI medical

images. In detail, the patient-specific images are processed with a particular approach based on a multi-compartment model, which separates the diffusion signal into a free-water (FW) and a tract-related, non-free-water (NFW) compartments [133]. This approach allows to overcome the limit of inaccurate estimation of white matter tract directions in regions with a high content of free water, such as cerebrospinal fluid or oedema. This is particularly important in our model to correctly estimate diffusion data in the region close to the brain ventricles. For this reason, initial data consist of 6 diffusion images, concerning only the non-free water component, which are assembled in a symmetric tensor called $\mathbb{D}^0_{\text{NFW}}$. Then, the initial diffusion tensor $\mathbb{D}^0$ is obtained from a weighted sum of two different contributions: an isotropic tensor, related to the unconstrained diffusion of substances in the free water, and the tensor constructed with DTI data, taking into account the diffusion limited by the tissue structures. Therefore, we set

$$\mathbb{D}^0 = \phi_\ell^0 \mathbb{D}^0_{\text{FW}} + (1 - \phi_\ell^0)\mathbb{D}^0_{\text{NFW}}\,, \tag{25}$$

where $\mathbb{D}^0_{\text{FW}} := D_w \mathbb{I}$, with D_w a scalar value which represents the diffusivity of free water at 37°C. The value $\phi_\ell^0(\mathbf{X})$ represents the liquid volumetric fraction at the initial time and it considers the fluid content in different regions of the brain. As a consequence, in regions where a high amount of liquid is present, diffusion is dominated by the purely isotropic free water component $\mathbb{D}^0_{\text{FW}}$, whereas more weight is given to diffusion along the white matter fibres in regions with reduced presence of fluid. Starting from the definition of Eq. (25), the diffusion tensor $\mathbb{D}$ at the current instant of time is derived from $\mathbb{D}^0$ by accounting for the fact that the growing tumour displaces the surrounding white matter fibres and thereby modifies the preferential directions of diffusion. We remark that such a change is only supposed to affect the non-free water component $\mathbb{D}^0_{\text{NFW}}$, while the free water one remains unaltered, i.e., $\mathbb{D}_{\text{FW}} \equiv \mathbb{D}^0_{\text{FW}}$. We also underline that the free water content evolves in time and space and it is here assumed to be equivalent to the fluid phase volume fraction $\phi_\ell(\mathbf{x}, t)$. With these observations in mind, if we call $\lambda_1^0 \geq \lambda_2^0 \geq \lambda_3^0$ the eigenvalues of $\mathbb{D}^0_{\text{NFW}}$ and $\mathbf{e}_1^0$, $\mathbf{e}_2^0$, $\mathbf{e}_3^0$ the corresponding orthonormal eigenvectors, we can define the current diffusion tensor as

$$\mathbb{D} = \phi_\ell \mathbb{D}_{\text{FW}} + (1 - \phi_\ell)\mathbb{D}_{\text{NFW}}\,, \tag{26}$$

where $\mathbb{D}_{\text{FW}} = D_w \mathbb{I}$, while $\mathbb{D}_{\text{NFW}}$ is constructed as follows:

$$\mathbb{D}_{\text{NFW}} = \sum_{i=1}^{3} \lambda_i^0 \frac{\mathbb{F}_{\text{s}}\mathbf{e}_i^0 \otimes \mathbb{F}_{\text{s}}\mathbf{e}_i^0}{\mathbf{e}_i^0 \cdot \mathbb{C}_{\text{s}}\mathbf{e}_i^0}\,. \tag{27}$$

The representation given by Eq. (27) stems from the discussions above and prescribes that each eigenvector of the initial diffusion tensor $\mathbb{D}^0_{\text{NFW}}$ is deformed through the solid deformation gradient $\mathbb{F}_{\text{s}}$, to account for possible alterations of the anisotropy directions following cancer expansion. Then, the deformed eigenvectors $\mathbb{F}_{\text{s}}\mathbf{e}_i^0$, $i = 1, 2, 3$, are normalised dividing by $|\mathbb{F}_{\text{s}}\mathbf{e}_i^0| = \sqrt{\mathbf{e}_i^0 \cdot \mathbb{C}_{\text{s}}\mathbf{e}_i^0}$, with $\mathbb{C}_{\text{s}} = \mathbb{F}_{\text{s}}^{\text{T}}\mathbb{F}_{\text{s}}$. Such a choice is motivated by the will of changing only the directions of diffusion while keeping the average diffusivity along the fibres, i.e. the trace of $\mathbb{D}_{\text{NFW}}$, unmodified in time. Indeed, a simple push-forward operation on $\mathbb{D}^0_{\text{NFW}}$ would result not only in a change of the preferential directions, but also in a change of diffusivity due to fibre extension or shortening. Therefore, in choosing an appropriate normalisation, we decided to preserve the average diffusivity. It is here important to emphasize that, given the definition of Eq. (27), a pullback of $\mathbb{D}_{\text{NFW}}$ to the reference configuration results in a tensor with the same eigenvectors as $\mathbb{D}^0_{\text{NFW}}$, but with different eigenvalues, due to the aforementioned modelling choices. Indeed, introducing $\mathbb{D}^*_{\text{NFW}}$, which is the tensor $\mathbb{D}_{\text{NFW}}$ mapped to the reference configuration

$$\begin{aligned}\mathbb{D}^*_{\text{NFW}} &:= J_{\text{s}}\mathbb{F}_{\text{s}}^{-1}\mathbb{D}_{\text{NFW}}\mathbb{F}_{\text{s}}^{-\text{T}} \\ &= \sum_{i=1}^{3} \frac{\lambda_i^0 J_{\text{s}}}{\mathbf{e}_i^0 \cdot \mathbb{C}_{\text{s}}\mathbf{e}_i^0}\mathbb{F}_{\text{s}}^{-1}(\mathbb{F}_{\text{s}}\mathbf{e}_i^0 \otimes \mathbb{F}_{\text{s}}\mathbf{e}_i^0)\mathbb{F}_{\text{s}}^{-\text{T}} \\ &= \sum_{i=1}^{3} \frac{\lambda_i^0 J_{\text{s}}}{\mathbf{e}_i^0 \cdot \mathbb{C}_{\text{s}}\mathbf{e}_i^0}\mathbf{e}_i^0 \otimes \mathbf{e}_i^0\,,\end{aligned} \tag{28}$$

the eigenvalues $\tilde{\lambda}_i$ of this tensor [23, 116] are

$$\tilde{\lambda}_i := \frac{\lambda_i^0 J_{\text{s}}}{\mathbf{e}_i^0 \cdot \mathbb{C}_{\text{s}}\mathbf{e}_i^0}\,, \qquad i = 1, 2, 3\,. \tag{29}$$

Finally, we note that, by defining the diffusion tensor weighted by ϕ_ℓ, we can effectively account for variations in intratumoral cellularity, which in turn influence the Apparent Diffusion Coefficient (ADC), a metric that reflects the magnitude of diffusion [8, 89, 105].

Permeability tensor $\mathbb{K}$. As much as diffusion, also the fluid motion due to pressure gradients follows some preferential directions, due to the anisotropic nature of brain tissue [168]. This information is encapsulated in the permeability tensor $\mathbb{K}$ appearing in Eqs. (5)–(12), which is also built from imaging data appropriately modified to account for tissue deformation. In particular, we can derive the permeability tensor $\mathbb{K}$ by using the information about the fibre directions contained in the tensor $\mathbb{D}^0_{\text{NFW}}$, namely the eigenvalues λ_1^0, λ_2^0, λ_3^0, and the eigenvectors $\mathbf{e}_1^0$, $\mathbf{e}_2^0$, and $\mathbf{e}_3^0$, suitably modified to account for tissue deformations, as is done for the diffusion tensor. Specifically, we define $\mathbb{K}$ as

$$\mathbb{K} = K(\phi_{\text{s}})\,\mathbb{A}\,, \tag{30}$$

where $K(\phi_s)$ is a proper function of the solid volume fraction and $\mathbb{A}$ is the *tensor of preferential directions*, reconstructed from the patient-specific DTI data.

In more detail, with the same procedure used for the definition of $\mathbb{D}_{\text{NFW}}$, we assume that $\mathbb{A}$ can be reconstructed from the eigenvectors of $\mathbb{D}^0_{\text{NFW}}$ deformed through the solid deformation gradient $\mathbb{F}_s$. However, in the case of the permeability tensor, the eigenvalues are rescaled to enhance the anisotropy along the fibres by appropriate anisotropy tuning functions as described in [2, 4, 94], and a normalisation is performed to preserve the mean permeability as done in [2, 4, 116]. Therefore, the tensor $\mathbb{A}$ is defined as

$$\mathbb{A} = \frac{1}{\mathrm{A}_{av}}\widehat{\mathbb{A}}\,, \quad \mathrm{A}_{av} = \frac{1}{3}\,\mathrm{tr}(\widehat{\mathbb{A}})\,, \tag{31}$$

$$\widehat{\mathbb{A}} = \tilde{a}_1(r)\lambda_1^0 \frac{\mathbb{F}_s\mathbf{e}_1^0 \otimes \mathbb{F}_s\mathbf{e}_1^0}{\mathbf{e}_1^0 \cdot \mathbb{C}_s\mathbf{e}_1^0} + \tilde{a}_2(r)\lambda_2^0 \frac{\mathbb{F}_s\mathbf{e}_2^0 \otimes \mathbb{F}_s\mathbf{e}_2^0}{\mathbf{e}_2^0 \cdot \mathbb{C}_s\mathbf{e}_2^0} + \tilde{a}_3(r)\lambda_3^0 \frac{\mathbb{F}_s\mathbf{e}_3^0 \otimes \mathbb{F}_s\mathbf{e}_3^0}{\mathbf{e}_3^0 \cdot \mathbb{C}_s\mathbf{e}_3^0}\,, \tag{32}$$

where the normalisation by A_{av} keeps the trace of $\mathbb{A}$ equal to 3 (as for the identity tensor), r is the anisotropy tuning parameter, and $\tilde{a}_i(r)$ are functions of r such that, if $r > 1$, anisotropy is enhanced (see [2, 4, 94] for further details). In order to understand the extent of anisotropy and to correctly define the functional forms of $\tilde{a}_i(r)$ allowing to represent scenarios of monodirectional, planar, and spherical growth as a consequence of the fibre orientation in the brain, we need to look at the eigenvalues $\tilde{\lambda}_i$, given by Eq. (29), of the deformed diffusion tensor $\mathbb{D}_{\text{NFW}}$ pulled back to the reference configuration, as defined in Eq. (28). We sort the eigenvalues $\tilde{\lambda}_i$ in descending order and introduce $\lambda_{\max} = \max\left\{\tilde{\lambda}_1, \tilde{\lambda}_2, \tilde{\lambda}_3\right\}$, $\lambda_{\min} = \min\left\{\tilde{\lambda}_1, \tilde{\lambda}_2, \tilde{\lambda}_3\right\}$ and λ_{mid} the remaining one. Then we calculate the linear, planar, and spherical anisotropy coefficients [94] respectively defined by

$$c_l := \frac{\lambda_{\max} - \lambda_{\text{mid}}}{\lambda_{\max} + \lambda_{\text{mid}} + \lambda_{\min}}\,, c_p := \frac{2(\lambda_{\text{mid}} - \lambda_{\min})}{\lambda_{\max} + \lambda_{\text{mid}} + \lambda_{\min}}\,,$$
$$c_s := \frac{3\lambda_{\min}}{\lambda_{\max} + \lambda_{\text{mid}} + \lambda_{\min}}\,, \tag{33}$$

and we introduce

$$a_{\max}(r) := rc_l + rc_p + c_s\,,\ a_{\text{mid}}(r) := c_l + rc_p + c_s\,,$$
$$a_{\min}(r) := c_l + c_p + c_s\,. \tag{34}$$

From the definition of c_l, c_p and c_s, we can observe that $a_{\min}(r) \equiv 1$. Finally, depending on the descending order of the eigenvalues $\tilde{\lambda}_i$, we associate $\tilde{a}_1(r)$, $\tilde{a}_2(r)$, and $\tilde{a}_3(r)$ with the corresponding coefficients between $a_{\max}(r), a_{\text{mid}}(r)$ and $a_{\min}(r)$. We observe that, similarly to the diffusion tensor, such a construction allows us to take advantage of the mechanical variables of the model to make the permeability evolve in time, enforcing the correct anisotropy, derived from the mechanical deformation. In this case as well, the eigenvectors of the tensor remapped to the reference configuration remain unchanged and are still represented by $\mathbf{e}_1^0$, $\mathbf{e}_2^0$ and $\mathbf{e}_3^0$.

As a functional form for the term $K(\phi_s)$, we will consider the exponential Holmes-Mow expression [21, 88], which is frequently used in the modelling of soft, hydrated biological structures [53, 54, 172]:

$$K(\phi_s) = k_0 \left[\frac{\phi_{sn}(1-\phi_s)}{\phi_s(1-\phi_{sn})}\right]^{\alpha_0} \exp\left(\frac{m}{2}\frac{\phi_{sn}^2 - \phi_s^2}{\phi_s^2}\right)\,, \tag{35}$$

being α_0 and m model parameters, and k_0 the reference permeability value. The choice of the coefficient $K(\phi_s)$ is motivated by the will of introducing a deformation-dependent permeability, which is not constant as the tumour grows and the tissue experiences stresses and strains. In particular, it is required that the permeability decreases as the solid volume fraction increases. The linearised version of Eq. (35) for small strains has often been adopted to describe the permeability of brain tissue [72, 144, 146, 176]. However, since we deal with finite deformations and nonlinear mechanics of the brain, we choose to use the nonlinear permeability of Eq. (35) as in a previous work [116], looking forward to further experimental confirmation for brain tissue.

Anisotropic growth tensor $\mathbb{F}_g$. Finally, we have to provide an expression for the tensor $\mathbb{F}_g$ that describes inelastic mechanical distortions related to growth. Recalling Eq. (22), we define it as follows:

$$\mathbb{F}_g = g_1\mathbf{e}_1^0 \otimes \mathbf{e}_1^0 + g_2\mathbf{e}_2^0 \otimes \mathbf{e}_2^0 + g_3\mathbf{e}_3^0 \otimes \mathbf{e}_3^0\,, \tag{36}$$

where $\mathbf{e}_1^0$, $\mathbf{e}_2^0$ and $\mathbf{e}_3^0$ are the eigenvectors of $\mathbb{D}^0_{\text{NFW}}$. Such a choice for the principal directions of growth deformation reflects the anisotropic structure of the tissue, with growth preferentially happening along the white matter tracts. This is a relevant difference from previous works on brain tumour growth since, as discussed before, $\mathbb{F}_g$ is often considered to be isotropic.

Given that the growth tensor has to match the condition of Eq. (20), and recalling Eq. (24), we need to prescribe the evolution in time of the stretch ratios g_1, g_2 and g_3 by means of a proper choice of the coefficients β_i, $i = 1, 2, 3$. This choice should take into account that white matter tracts and other physical structures in the brain (such as vessels) are used by tumour cells to expand along preferential directions. The tumour expansion is dictated not only by cell migration, but also by cell division/growth. Therefore, we define the coefficients β_i, $i = 1, 2, 3$ in order to enhance cell growth along the principal directions of the brain physical structures, which can be determined through the eigenvectors of the $\mathbb{D}^0_{\text{NFW}}$ tensor inferred from DTI data. Then, as done for the permeability

tensor, we assume that the extent of growth in each direction is related to the eigenvalue of the deformed diffusion ellipsoid associated with that growth direction, possibly rescaled by a factor to enhance anisotropic growth. Specifically, we will consider the following evolution equations and initial conditions:

$$\frac{\dot{g_1}}{g_1} = \frac{\tilde{\lambda}_1\tilde{a}_1(r)}{\tilde{\lambda}_1\tilde{a}_1(r)+\tilde{\lambda}_2\tilde{a}_2(r)+\tilde{\lambda}_3\tilde{a}_3(r)}\frac{\Gamma_s}{\phi_s}, \quad \text{with } g_1(0)=1\,, \tag{37a}$$

$$\frac{\dot{g_2}}{g_2} = \frac{\tilde{\lambda}_2\tilde{a}_2(r)}{\tilde{\lambda}_1\tilde{a}_1(r)+\tilde{\lambda}_2\tilde{a}_2(r)+\tilde{\lambda}_3\tilde{a}_3(r)}\frac{\Gamma_s}{\phi_s}, \quad \text{with } g_2(0)=1\,, \tag{37b}$$

$$\frac{\dot{g_3}}{g_3} = \frac{\tilde{\lambda}_3\tilde{a}_3(r)}{\tilde{\lambda}_1\tilde{a}_1(r)+\tilde{\lambda}_2\tilde{a}_2(r)+\tilde{\lambda}_3\tilde{a}_3(r)}\frac{\Gamma_s}{\phi_s}, \quad \text{with } g_3(0)=1\,, \tag{37c}$$

where $\tilde{\lambda}_1$, $\tilde{\lambda}_2$ and $\tilde{\lambda}_3$ are defined in Eq. (29) and $\tilde{a}_1(r)$, $\tilde{a}_2(r)$, and $\tilde{a}_3(r)$ are obtained by association with $a_{\max}(r)$, $a_{\mathrm{mid}}(r)$ and $a_{\min}(r)$ defined by Eq. (34), through the same permutation required to sort the eigenvalues $\tilde{\lambda}_i$ in descending order. Consequently, the choice of the β_i coefficients is closely related to the eigenvalues $\tilde{\lambda}_i$, which are tied to the biomechanical properties of the tumour and its interaction with the surrounding tissue, reflecting the impact of tumour-induced deformations on the eigenvalues. We remark that the mathematical assumption for the choice of the β_i is grounded on the idea that the alignment of the cell mitotic spindle during cell division is guided by the physical structures in the surrounding environment. This hypothesis has been tested (mathematically and biologically) in other anisotropic environments (see for example the work of Hoehme et al. for the liver [85]) and needs to be validated by experimental tests for brain tissue. For the sake of completeness, we note that other assumptions that take into account, for instance, the stress experienced by cells in a particular direction can be considered [81].

2.3 Interface, boundary, and initial conditions

Before solving the model to describe brain tumour growth, we need to provide appropriate conditions at the interface between the tumour and the host tissue, as well as boundary and initial conditions.

Interface conditions at the boundary $\partial\Omega_t^*$ between the tumour and the healthy tissue. First of all, we have to define proper conditions on the material interface $\partial\Omega_t^*$ between the tumour and the host healthy tissue. In particular, as done in [23], we prescribe continuity of the displacement of the solid phase, of the normal stress, of the fluid pressure, of the nutrients' concentration, and of fluid and chemical fluxes at the interface. Therefore, the conditions that we impose on $\partial\Omega_t^*$ are the following:

$$[\![\mathbf{u}_s]\!]|_{\partial\Omega_t^*} = \mathbf{0}\,, \tag{38a}$$

$$\left[\!\!\left[\frac{\mathbb{K}^*}{\mu}\,\mathrm{Grad}\,p\cdot\mathbf{N}\right]\!\!\right]|_{\partial\Omega_t^*} = 0\,, \tag{38b}$$

$$[\![\mathbb{P}_s\mathbf{N}]\!]|_{\partial\Omega_t^*} = \mathbf{0}\,, \tag{38c}$$

$$[\![p]\!]|_{\partial\Omega_t^*} = 0\,, \tag{38d}$$

$$[\![c_n]\!]|_{\partial\Omega_t^*} = 0\,, \tag{38e}$$

$$[\![\phi_\ell\mathbb{D}^*\,\mathrm{Grad}\,c_n\cdot\mathbf{N}]\!]\big|_{\partial\Omega_t^*} = 0\,, \tag{38f}$$

where $[\![\cdot]\!]|_{\partial\Omega_t^*}$ denotes the jump across the interface and $\mathbf{N}$ is the unit normal vector to $\partial\Omega_t^*$ pointing outwards. In particular, we underline that the condition of Eq. (38c) is obtained by combining the continuity across the interface of the total stress $\mathbb{P} = -J_s p\mathbb{F}_s^{-\mathrm{T}} + \mathbb{P}_s$ in the normal direction and the continuity of the pressure p. Furthermore, we remark that the continuity of the solid displacement vector in Eq. (38a) follows by combining the continuity of the normal velocity $\mathbf{v}_s\cdot\mathbf{N}$ with the continuity of the tangential component of the same velocity field. The former is a natural condition to avoid rupture and detachment within the tissue. At the same time, due to the presence in biological tissues of cell-cell and cell-extracellular matrix adhesion molecules (mainly cadherins and integrins), it is physically reasonable to assume that tangential displacements (and thus velocities) at the tumour-healthy tissue boundary are also continuous. These biologically consistent observations lead to the assumption of continuous displacement $\mathbf{u}_s$ across the interface. However, we remark that the continuity of the displacement field does not necessarily imply that the solid deformation gradient $\mathbb{F}_s$ and its determinant J_s are continuous. Finally, we observe that, without this requirement, appropriate conditions describing the slipping at the tumour-host interface, possibly taking into account the attachment/detachment of bonds, should be defined. Furthermore, in the case of discontinuous tangential displacements, the healthy tissue boundary should be defined and meshed separately from the tumour boundary to allow the two surfaces to deform in different ways.

Boundary conditions. Before imposing the boundary conditions, it is important to remark (see Fig. 1) that the boundary of our domain $\partial\Omega^* = \partial\Omega_{\mathrm{out}}^* \cup \partial\Omega_v^*$ is composed by the external boundary $\partial\Omega_{\mathrm{out}}^*$, corresponding to the cranial skull, and by the edges of brain ventricles $\partial\Omega_v^*$. Specifically, in our simulations for tumour growth in the brain, we consider the following boundary conditions on $\partial\Omega_{\mathrm{out}}^*$:

$$\mathbf{u}_s = \mathbf{0} \qquad \text{on } \partial\Omega_{\mathrm{out}}^*\,, \quad \forall t\in(0,T)\,, \tag{39a}$$

$$\mathbb{K}^*\,\mathrm{Grad}\,p\cdot\mathbf{N} = 0 \qquad \text{on } \partial\Omega_{\mathrm{out}}^*\,, \quad \forall t\in(0,T)\,, \tag{39b}$$

$$c_n = 1 \qquad \text{on } \partial\Omega_{\mathrm{out}}^*\,, \quad \forall t\in(0,T)\,. \tag{39c}$$

In detail, we impose a null Dirichlet boundary condition for the displacement $\mathbf{u}_s$, given that the skull is fixed. For what

concerns the pressure p, we take into account a Neumann boundary condition since we assume that fluid cannot flow outside the skull. Finally, for the nutrients' concentration, we suppose that the brain boundary is sufficiently far from the tumour, so we can assume that the oxygen concentration is maintained constant at the physiological value, leading to the condition (39c) for the normalized concentration.

Instead, on the boundary of the ventricles $\partial\Omega_{\mathrm{v}}^*$ we impose the continuity of the stresses and an outflow boundary condition for the chemical mass to model an outlet where the species can leave the domain with the fluid flow, i.e.,

$$\mathbb{P}_{\mathrm{s}}\mathbf{N} = \mathbf{0} \qquad \text{on } \partial\Omega_{\mathrm{v}}^*\,, \quad \forall t \in (0,T)\,, \tag{40a}$$

$$p = p_{\mathrm{v}} \qquad \text{on } \partial\Omega_{\mathrm{v}}^*\,, \quad \forall t \in (0,T)\,, \tag{40b}$$

$$\phi_\ell \mathbb{D}^* \operatorname{Grad} c_n \cdot \mathbf{N} = 0 \qquad \text{on } \partial\Omega_{\mathrm{v}}^*\,, \quad \forall t \in (0,T)\,. \tag{40c}$$

The first and second conditions are a consequence of the continuity of stresses imposed at the ventricles' interface, which leads to a boundary condition that involves only the constitutively determined part of the first Piola-Kirchhoff stress tensor $\mathbb{P}_{\mathrm{s}}$, and to the condition (40b) that enforces a fixed value for the pressure equal to the physiological intracranial pressure p_{v} on $\partial\Omega_{\mathrm{v}}^*$. This condition takes into account the capability of the interconnected brain ventricular system to maintain a physiological pressure. Furthermore, for c_n we consider an outflow boundary condition [107], considering that mass transfer at the outlet boundary only happens by convection, while the net diffusive flux is negligible. This condition implies that the fluid is flowing across the boundary (at an unchanged velocity along the normal direction) and that the local concentration of chemicals on either side of the brain-ventricle interface is equal, so that the normal component of the chemical species gradient is zero at $\partial\Omega_{\mathrm{v}}^*$. This condition may be reasonable in the absence of physical barriers that could impede fluid and mass transport across the ventricles and maintain different chemical concentrations on either side. More complex conditions may require a detailed description of the hydrodynamics of the ventricles, taking into account washout and uptake of chemicals.

Initial conditions. At the beginning of the tumour growth process, we assume that the displacement and the pressure are equal to zero. In addition, we take the scalar fields g_1, g_2 and g_3 as equal to 1 everywhere in the tumour domain at $t = 0$. The volumetric fraction of the cell phase is instead initialized to a value $\phi_{\mathrm{s}}^0(\mathbf{X})$, whose estimate will be discussed in Sect. 3.2. Finally, in order to obtain the initial nutrients concentration $c_n^0(\mathbf{X})$, we solve the steady version of the nutrients governing equation, neglecting advection:

$$-\operatorname{Div}\left[\phi_\ell \mathbb{D}^0 \operatorname{Grad} c_n^0\right] = J_{\mathrm{s}} G_n\,. \tag{41}$$

In conclusion, we have the following set of initial conditions:

$$\mathbf{u}_{\mathrm{s}}(\mathbf{X},0) = \mathbf{0}\,, \qquad \forall \mathbf{X} \in \Omega^*\,, \tag{42a}$$

$$p(\mathbf{X},0) = 0\,, \qquad \forall \mathbf{X} \in \Omega^*\,, \tag{42b}$$

$$g_i(\mathbf{X},0) = 1\,,\ i = 1,2,3\,, \qquad \forall \mathbf{X} \in \Omega^*\,, \tag{42c}$$

$$\phi_{\mathrm{s}}(\mathbf{X},0) = \phi_{\mathrm{s}}^0(\mathbf{X})\,, \qquad \forall \mathbf{X} \in \Omega^*\,, \tag{42d}$$

$$c_n(\mathbf{X},0) = c_n^0(\mathbf{X})\,, \qquad \forall \mathbf{X} \in \Omega^*\,. \tag{42e}$$

3 Numerical implementation

The set of equations governing the evolution of the system in the domain Ω_{t}^* consists of Eqs. (1), (5), (13), (14), (21), (37). These equations and the constitutive assumptions (17) still hold in the healthy domain, recalling that in the healthy region we assume $\mathbb{F}_{\mathrm{g}} = \mathbb{I}$, which means $\dot{g}_i = 0\,,\ i = 1,2,3$.

The system allows to determine all the unknown fields, namely, the displacement field $\mathbf{u}_{\mathrm{s}}(\mathbf{X},t)$ and the scalar fields $p(\mathbf{X},t)$, $\phi_{\mathrm{s}}(\mathbf{X},t)$, $\phi_\ell(\mathbf{X},t)$, $g_1(\mathbf{X},t)$, $g_2(\mathbf{X},t)$, $g_3(\mathbf{X},t)$ and $c_n(\mathbf{X},t)$, $\forall \mathbf{X} \in \Omega^* = \Omega_{\mathrm{t}}^* \cup \Omega_{\mathrm{h}}^*$ and $\forall t \in (0,T)$, equipped with the boundary and interface conditions discussed in Sect. 2.3.

In this Section, we discuss how the Lagrangian model for brain tumour growth is solved through numerical simulations. The weak formulation of the model is derived in Appendix A. The discretization in time and space of the weak formulation is instead reported and summarised in Sect. 3.1. Finally, in Sect. 3.2, we assess the values of the parameters that appear in the system.

3.1 Discrete formulation of the continuous variational problems

In order to implement our model and solve the equations by means of the Finite Element Method, it is customary to introduce a discrete formulation in time and space of the continuous variational problems derived in Appendix A, namely, Eqs. (A.12) and (A.15). We make use of linear tetrahedron $\mathbb{P}_1$ elements, so we introduce the following finite element spaces:

$$\boldsymbol{V}_{h,\mathrm{out}} := \Big\{ \boldsymbol{q}_h \in \left[C^0\left(\overline{\Omega^*}\right)\right]^3 : \boldsymbol{q}_h\big|_K \in [\mathbb{P}_1(K)]^3 \quad \forall K \in \mathcal{T}_h,\ \boldsymbol{q}_h = \mathbf{0} \text{ on } \partial\Omega_{\mathrm{out}}^* \Big\} \subset \boldsymbol{H}^1_{0,\partial\Omega_{\mathrm{out}}^*}\left(\Omega^*\right)\,,$$

$$W_{h0,\mathrm{out}} := \Big\{ q_h \in C^0\left(\overline{\Omega^*}\right) : q_h\big|_K \in \mathbb{P}_1(K) \quad \forall K \in \mathcal{T}_h,\ q_h = 0 \text{ on } \partial\Omega_{\mathrm{out}}^* \Big\} \subset H^1_{0,\partial\Omega_{\mathrm{out}}^*}\left(\Omega^*\right)\,,$$

$$W_{h0,\mathrm{v}} := \Big\{ q_h \in C^0\left(\overline{\Omega^*}\right) : q_h\big|_K \in \mathbb{P}_1(K)$$

$$\forall K \in \mathcal{T}_h,\ q_h = 0 \text{ on } \partial\Omega^*_{\mathrm{v}} \Big\} \subset H^1_{0,\partial\Omega^*_{\mathrm{v}}}\left(\Omega^*\right),$$

$$W_{h1,\mathrm{out}} := \Big\{ q_h \in C^0\left(\overline{\Omega^*}\right) : q_h|_K \in \mathbb{P}_1(K)$$

$$\forall K \in \mathcal{T}_h,\ q_h = 1 \text{ on } \partial\Omega^*_{\mathrm{out}} \Big\} \subset H^1\left(\Omega^*\right),$$

$$W_{hp_{\mathrm{v}},\mathrm{v}} := \Big\{ q_h \in C^0\left(\overline{\Omega^*}\right) : q_h|_K \in \mathbb{P}_1(K)$$

$$\forall K \in \mathcal{T}_h,\ q_h = p_{\mathrm{v}} \text{ on } \partial\Omega^*_{\mathrm{v}} \Big\} \subset H^1\left(\Omega^*\right),$$

where $\mathcal{T}_h$ is a decomposition of the domain Ω^* into tetrahedra K conforming to the tumour boundary.

For what concerns the time discretization, given N time instants on the interval $(0, T)$, $\Delta t := T/N$ is the time step and we use a superscript k to denote the value of a quantity at time $t_k = k\Delta t$. Moreover, we use the superscript $k+1$ to denote the value of a quantity of interest at the next time step.

First, we have to introduce a proper discretisation of the ordinary differential equations for g_1, g_2 and g_3 in (37). Let $g^{k+1}_{1,h}$, $g^{k+1}_{2,h}$, $g^{k+1}_{3,h}$ be piecewise-constant functions defined on Ω^* approximating g_1, g_2, g_3, respectively. The equations of the system (37) are discretized in time using an explicit Euler method, only in the nodes which belong to the tumour domain Ω^*_{t}:

$$g^{k+1}_{i,h} = g^k_{i,h}\left(1 + \Delta t \frac{\tilde{\lambda}^k_i \tilde{a}^k_i(r)}{\tilde{\lambda}^k_1 \tilde{a}^k_1(r) + \tilde{\lambda}^k_2 \tilde{a}^k_2(r) + \tilde{\lambda}^k_3 \tilde{a}^k_3(r)} \frac{\Gamma_{\mathrm{s}}(c^k_h, \phi^k_{\mathrm{s},h})}{\phi^k_{\mathrm{s},h}}\right), \quad i = 1, 2, 3, \tag{43}$$

where $\tilde{\lambda}_i$ and $\tilde{a}_i(r)$ are respectively the eigenvalues and the coefficients of Eqs. (34) and (29) computed with the information acquired at time step k.

We can then formulate the discrete variational problem for $\mathbf{u}^{k+1}_h$ and p^{k+1}_h as follows: for $k = 1, \ldots, N$, given $\left(\mathbf{u}^k_h, p^k_h\right) \in \boldsymbol{V}_{h,\mathrm{out}} \times W_{hp_{\mathrm{v}},\mathrm{v}}$ find $\left(\mathbf{u}^{k+1}_h, p^{k+1}_h\right) \in \boldsymbol{V}_{h,\mathrm{out}} \times W_{hp_{\mathrm{v}},\mathrm{v}}$ such that $\forall (\mathbf{v}_h, w_h) \in \boldsymbol{V}_{h,\mathrm{out}} \times W_{h0,\mathrm{v}}$ it holds

$$\left(J_{\mathrm{s}}\left(\mathbf{u}^{k+1}_h\right), w_h\right) + \Delta t \left(\mathrm{Grad}\, w_h, \frac{\mathbb{K}^*\left(\mathbf{u}^{k+1}_h\right)}{\mu} \mathrm{Grad}\, p^{k+1}_h\right) +$$
$$- \left(\mathbb{P}\left(\mathbf{u}^{k+1}_h, p^{k+1}_h\right), \mathrm{Grad}\, \mathbf{v}_h\right) - \left(J_{\mathrm{s}}\left(\mathbf{u}^{k+1}_h\right) p_{\mathrm{v}} \mathbb{F}_{\mathrm{s}}^{-\mathrm{T}}\left(\mathbf{u}^{k+1}_h\right) \mathbf{N}, \mathbf{v}_h\right)_S =$$
$$= \left(J_{\mathrm{s}}\left(\mathbf{u}^k_h\right), w_h\right), \tag{44}$$

where we have used an implicit method for time integration. For simplicity, we have denoted by $(\cdot, \cdot)$ the standard scalar product on the spaces $L^2(\Omega^*)$, $L^2(\Omega^*; \mathbb{R}^3)$ and $L^2(\Omega^*; \mathbb{R}^{3\times 3})$ when appropriate, and by $(\cdot, \cdot)_S$ the integral on the surface $\partial\Omega^*_{\mathrm{v}}$.

Afterwards, we need to introduce adequate discretisation of the mass balance (21) and the saturation condition (1), where $\phi^{k+1}_{\mathrm{s},h}$ and $\phi^{k+1}_{\ell,h}$ represent piecewise-constant functions approximating ϕ_{s} and ϕ_ℓ. The first equation is discretized as

$$\phi^{k+1}_{\mathrm{s},h} = J_{\mathrm{s}}^{-1}(\mathbf{u}^{k+1}_h) g^{k+1}_{1,h} g^{k+1}_{2,h} g^{k+1}_{3,h} \phi_{\mathrm{sn}}\,. \tag{45}$$

Once we have computed $\phi^{k+1}_{\mathrm{s},h}$, we can derive $\phi^{k+1}_{\ell,h}$ using the saturation condition

$$\phi^{k+1}_{\ell,h} = 1 - \phi^{k+1}_{\mathrm{s},h}\,. \tag{46}$$

Finally, we can solve the variational problem for the nutrients. Given $c^k_h \in W_{h1,\mathrm{out}}$, we have to find $c^{k+1}_h \in W_{h1,\mathrm{out}}$ such that $\forall q_h \in W_{h0,\mathrm{out}}$ it holds

$$\left(J_{\mathrm{s}}\left(\mathbf{u}^{k+1}_h\right) c^{k+1}_h, q_h\right) - \Delta t \left(\frac{\mathbb{K}^*\left(\mathbf{u}^{k+1}_h\right)}{\mu \phi^{k+1}_\ell} \mathrm{Grad}\, p^{k+1}_h \cdot \mathrm{Grad}\, c^{k+1}_h, q_h\right) +$$
$$+ \Delta t \left(\mathrm{Grad}\, q_h, \mathbb{D}^*\left(\mathbf{u}^{k+1}_h\right) \mathrm{Grad}\, c^{k+1}_h\right) - \Delta t \left(J_{\mathrm{s}}\left(\mathbf{u}^{k+1}_h\right) \frac{G_n\left(c^{k+1}_h\right)}{\phi^{k+1}_\ell}, q_h\right) =$$
$$= \left(J_{\mathrm{s}}\left(\mathbf{u}^{k+1}_h\right) c^k_h, q_h\right). \tag{47}$$

Also in this case, we have used an implicit Euler method for time integration. Furthermore, an adaptive time-step was used in order to ensure the convergence of the numerical simulations. Specifically, our equations are solved with a constant time-step, but if, at any given temporal instance, our method does not converge, Δt is halved until convergence is achieved. Once the next time-step is reached, the time-step is reset to the initial value.

3.2 Parameters estimation

Before running numerical simulations, it is essential to identify suitable values for the parameters involved in the model. While obtaining precise estimates for these parameters can be challenging, selecting reasonable values is crucial to generate a realistic outcome, which is one of the goals of our work. The selected parameter values, together with the biological ranges found in the literature and the relative references, are summarised in Table 1.

In particular, for the majority of the parameters, we have referred to the discussion presented in [23, 116], where a thorough estimation of parameters for brain tumour growth has been carried out. For what concerns the mechanical parameters $\mu_{1\mathrm{h}}$ and $\mu_{2\mathrm{h}}$ of the healthy tissue, we refer to the estimates of mean values provided by Balbi et al. for human brain matter [22], that is, we take $\mu_{1\mathrm{h}} = 3.06 \times 10^{-4}$ MPa and $\mu_{2\mathrm{h}} = 5.94 \times 10^{-4}$ MPa. These parameters are also in the range found by other authors [37, 38], even though also smaller values of the order of 10^{-5} MPa are sometimes

Table 1 List of the values of the model parameters employed in the numerical simulations

Parameter	Description	Value	Biological range	References
μ_{1h}	Mooney-Rivlin material parameter (healthy)	3.06×10^{-4} MPa	$3.0 \times 10^{-7}-6.436 \times 10^{-4}$ MPa	[22]
μ_{2h}	Mooney-Rivlin material parameter (healthy)	5.94×10^{-4} MPa	$1.1936 \times 10^{-4}-1.42058 \times 10^{-3}$ MPa	[22]
κ_h	Volumetric modulus (healthy)	1.389×10^{-4} MPa	$2 \times 10^{-4}-2 \times 10^{-2}$ MPa	[135]
μ_{1t}	Mooney-Rivlin material parameter (tumour)	3.06×10^{-3} MPa	$10^{-5}-10^{-2}$ MPa	[44, 124, 149]
μ_{2t}	Mooney-Rivlin material parameter (tumour)	5.94×10^{-3} MPa	–	[44, 124, 149]
κ_t	Volumetric modulus (tumour)	1.389×10^{-3} MPa	–	[135]
ν	Cell proliferation constant	0.65 day^{-1}	$0.5-1$ day^{-1}	[69]
c_0	Hypoxia threshold	0.30	0.15–0.5	[2]
ζ	Nutrients consumption rate	8640 day^{-1}	$8640-15650$ day^{-1}	[47, 116]
S_n	Nutrients supply rate	10^4 day^{-1}	–	[2, 42, 47]
ϕ_{sn}	Cell volume fraction in the natural state	0.45	0.3–0.5	[36]
ϕ_{max}	Maximum cell volume fraction	0.95	0.8–1	[23, 116]
D_w	Diffusivity of free water at 37°	259.2 $\text{mm}^2 \cdot \text{day}^{-1}$	$43.2-259.2$ $\text{mm}^2 \cdot \text{day}^{-1}$	[108]
k_0/μ	Hydraulic conductivity	7.8×10^4 $\text{mm}^2 \cdot \text{MPa}^{-1} \cdot \text{day}^{-1}$	10^4-10^5 $\text{mm}^2 \cdot \text{MPa}^{-1} \cdot \text{day}^{-1}$	[96]
α_0	Holmes-Mow permeability parameter	0.0848	–	[54]
m	Holmes-Mow permeability parameter	4.638	–	[54]
R_{eff}	Radiotherapy death rate	0.0648 day^{-1}	$0.06-0.0792$ day^{-1}	[2, 134, 138, 139]
k_{C1}	Concomitant CHT death rate	0.00735 day^{-1}	–	[2, 134, 138, 139]
k_{C2}	First cycle of adjuvant CHT death rate	0.0147 day^{-1}	–	[2, 134, 138, 139]
k_{C3}	Other cycles of adjuvant CHT death rate	0.0196 day^{-1}	–	[2, 134, 138, 139]
λ_c	Chemotherapy decay rate	0.05 day^{-1}	–	Estimated
p_v	Pressure exerted by cerebrospinal fluid	6.67×10^{-4} MPa	$0-1.3332 \times 10^{-3}$MPa	[6, 17]

found. Regarding the tumour, the choice of material parameters for brain cancer is debated in the literature. Several studies point out that the tumour is stiffer than the healthy tissue, even more than ten times in some cases [3, 44, 45, 124, 149, 153]. However, some works suggest that brain tumours may be as stiff as the normal tissue, or even softer [128, 157]. A study of different values for the mechanical parameters of healthy and tumour tissue was carried out computationally in [116]. In the present work, we choose $\mu_{1\mathrm{t}}$ and $\mu_{2\mathrm{t}}$ as ten times greater than their healthy counterparts. Ideally, these parameters could be estimated by means of patient-specific Magnetic Resonance Elastography (MRE), as done in [81]. However, accurate tools for the reconstruction of complex nonlinear constitutive responses by means of MRE are still lacking. The volumetric moduli κ_{t} and κ_{h} are also difficult to be estimated, given that very few experiments are carried out by accounting for poroelastic effects. Following [135], we take $\kappa_{\mathrm{h}} = 1.389 \times 10^{-4}$ MPa, and $\kappa_{\mathrm{t}} = 10\kappa_{\mathrm{h}}$. We remark that we choose not to differentiate the mechanical parameters between grey and white matter. Although some experiments showed rheological differences between them [39, 78], some subsequent investigations such as [38] do not seem to underline a substantial distinction. Furthermore, since in the present work we are focusing on a tumour which is ten times stiffer than the healthy tissue, the possible mechanical difference between grey and white matter appears to be less relevant. Therefore, we decided to prioritize simplicity and computational efficiency in the present version of the model, so we did not adopt this differentiation, which could have a greater impact if the cancer and the healthy tissue have comparable stiffness.

The parameter ν appearing in Eq. (7) is estimated as in [47] by using typical proliferation times for glioma cells in vitro, which range between 24 and 48 h. Hence, we choose an intermediate value of $\nu = 0.65\,\mathrm{day}^{-1}$. The hypoxia threshold c_0 is set to 0.30, given that values in the literature range from 0.15 to 0.5 [2, 69, 73, 163]. The nutrients consumption rate ζ in Eq. (7) is estimated as done in [47], resorting to measurements of oxygen diffusion in the brain. In particular, we set $\zeta = 8640\,\mathrm{day}^{-1}$. Instead, for the nutrients supply rate S_n, we refer to the value of $10^4\ \mathrm{days}^{-1}$ proposed in [42], as also done in [2, 23, 47, 116]. The maximum cell volume fraction $\phi_{\max}$, representing contact inhibition of cell growth, is set to be $\phi_{\max} = 0.95$. Even if, to the best of our knowledge, such a parameter is not estimated experimentally, we assume that a minimum amount of extracellular fluid remains present in the tissue, since we are not considering the formation of calcification and necrotic regions.

Then, we need to estimate the values of the parameters that appear in the radiotherapy and chemotherapy terms defined in Eq. (8). Inspired by the standard Stupp protocol [151] and recalling Eq. (10), we take the dose of radiation for every fraction d equal to 2 Gy, given once daily, i.e. $n = 1\ \mathrm{day}^{-1}$. Furthermore, the dose at which the contributions from the first and the second term in Eq. (10) are equal is given by α/β [Gy], which is an inverse measure of a tissue's sensitivity to the dosage administered during each treatment. In the following, the value prescribed in [134, 138] is used, where this ratio is taken as equal to 10 Gy. For what concerns the linear coefficient for RT-induced cell killing, we assume a value of $\alpha = 0.027\ \mathrm{Gy}^{-1}$, in agreement with [2, 134, 139]. As a consequence, we have that $\beta = 0.0027\ \mathrm{Gy}^{-2}$. Introducing all these parameters in Eq. (10), we obtain the value of the radiotherapy death rate $R_{\mathrm{eff}} = 0.0648\ \mathrm{day}^{-1}$. On the other hand, the values of CHT-induced cell killing rate are chosen with reference to [2, 134], i.e. $k_{C1} = 0.00735\ \mathrm{day}^{-1}$, $k_{C2} = 0.0147\ \mathrm{day}^{-1}$ and $k_{C3} = 0.0196\ \mathrm{day}^{-1}$. Finally, in the simulations where therapy decay is accounted for as in Eq. (11), we consider a value of $\lambda_c = 0.05\ \mathrm{day}^{-1}$. We remark that such a choice is not motivated by the will of reproducing the chemotherapeutic drug half life, which is indeed much shorter [70]. Instead, it is rather made with the intention of capturing the prolonged effects of chemotherapy over time. This allows to incorporate in our model the processes initiated by the drug and their effects on the tumour, in terms of cell late apoptosis, which gradually decline over time. Indeed, late apoptosis/necrosis induced by TMZ has been experimentally recorded even after many days from the last treatment [30, 83, 141]. However, we acknowledge that the correct estimation of such a parameter deserves further experimental studies and medical data.

Regarding the free water diffusivity coefficient D_w at 37°C, which appears in Eqs. (25) and (26), the mean value reported in the literature is $D_w = 259.2\ \mathrm{mm}^2\,\mathrm{day}^{-1}$ [108], and we decide to adopt such a value. Furthermore, it is necessary to estimate the cell volumetric fraction $\phi_{\mathrm{s}}^0(\mathbf{X})$ at the initial time. We assume it to be equal to the cell volumetric fraction in the natural state, denoted as ϕ_{sn}, which is a predefined constant. In this study, we consider a value of $\phi_{\mathrm{sn}} = 0.45$, based on the approximate estimation that the extracellular space, which is complementary to the solid volume fraction, constitutes around $50 - 60\%$ [36]. By prescribing $\phi_{\mathrm{s}}^0(\mathbf{X})$, we also define the initial fluid volumetric fraction $\phi_{\ell}^0(\mathbf{X}) = 1 - \phi_{\mathrm{s}}^0(\mathbf{X}) = 1 - \phi_{\mathrm{sn}}$, which is utilized in the construction of the initial diffusion tensor of Eq. (25). We remark that, although an ideal approach would involve the use of a voxel-wise estimation of the free-water content to determine a spatially dependent initial value for ϕ_{ℓ}^0 [8, 89], in this work we have chosen not to consider it for specific reasons. Firstly, the impact of this simplification on the results is not remarkable, as it is greatly mitigated by the exclusion of the ventricular region from our domain. In fact, the ventricles are mainly filled with water and therefore the inclusion of this area in the computational domain would have been most affected by this choice. Furthermore, in the specific region where the brain tumour was initially

localised, we identified a homogeneous distribution of the free water estimated from the DTI data. Moreover, to account for a spatially inhomogeneous distribution of ϕ_ℓ, it would be necessary to address an initial mechanical problem to establish the condition of mechanical equilibrium, in order to avoid tissue evolution unrelated to growth. Finally, simulations with highly inhomogeneous conditions face numerical convergence problems that require further analysis. Regarding the permeability parameters of Eq. (35), we remark that the reference permeability k_0 has units of mm^2, while in the literature it is frequent to estimate the hydraulic conductivity $k_c := k_0/\mu$, with μ the dynamic viscosity. Values for k_c, which has units $\text{mm}^2\ \text{MPa}^{-1}\ \text{day}^{-1}$, range in the literature between $10^4 - 10^5\ \text{mm}^2\ \text{MPa}^{-1}\ \text{day}^{-1}$ for the brain [20, 26, 96, 122, 168, 169]. We adopt the value of $k_c = 7.8 \times 10^4\ \text{mm}^2\ \text{MPa}^{-1}\ \text{day}^{-1}$, as in [96]. Instead, we take $\alpha_0 = 0.0848$ and $m = 4.638$ as for other soft tissues [54, 88], though specific experimental estimates for them in the brain are still lacking.

Finally, it is necessary to estimate the pressure p_v of cerebrospinal fluid (CSF) in the brain ventricles, which appears in the boundary condition (40b). Intracranial pressure measurements suggest that normal mean pressure exerted by CSF is in the range of 0 to 10 mmHg [6, 17]. We consider therefore an intermediate value within this range, i.e. 5 mmHg, which is equivalent to a value of $p_\text{v} = 6.67 \times 10^{-4}$ MPa. To be precise, this value could have also been set to zero as it merely causes a shift in pressure.

4 Results and discussion

The mechanical model used in our study simulates the progression of brain tumours to determine their preferential directions of growth and the resulting stresses and strains on the healthy surrounding brain tissue. The tumour is considered as a sphere of initial radius 2.5 mm, located near the right lateral ventricle of the brain. The evolution is then simulated for a time period of 140 days, both with and without therapies. In this way, we are able to evaluate how the growth and the mechanical alterations provoked by the tumour may adversely impact on the cerebral ventricles. Moreover, we can test different therapeutic protocols in the simulations and observe the consequences on cancer growth. Simulations have been performed using the discrete formulation described in Sect. 3.1, implemented in the software *FEniCS* [10, 113], which provides a high-level Python and C++ interface for solving PDEs through the Finite Element Method.

4.1 Simulation without any therapeutic intervention

A first simulation is performed without including neither radiotherapy nor chemotherapy, so the tumour is free to grow. Figure 3a illustrates the temporal progression of the solid cell fraction on the brain geometry. As cancer cells proliferate within the tumour region, there is a noticeable increase in the volumetric fraction occupied by the solid phase. After an uninterrupted growth period of approximately five months, ϕ_s approaches a value of 0.85 within the tumour domain, indicating a higher density of cancer cells as the tumour evolves. From Fig. 3, it is evident that the volumetric fraction of the cell phase, ϕ_s, exhibits an anisotropic expansion, extending beyond the tumour region and into the surrounding healthy tissue. This expansion is primarily driven by the compressive effects exerted by the expanding tumour mass on the neighbouring healthy region and ventricle. Conversely, a decrease in ϕ_s is observed near the ventricles, indicating an increased presence of the liquid phase in that specific zone and fluid flow near the compressed ventricles. These observations highlight the spatial heterogeneity of tumour-induced changes in the cell phase and the influence of neighbouring structures on these alterations. For what concerns the magnitude of the displacement $\|\mathbf{u}_\text{s}\|$ shown in Fig. 3b, it is immediately evident a substantial anisotropic growth behaviour, which follows the orientation of the surrounding white matter tracts. We can observe that values of the displacement are not negligible, since they reach a maximum value of 9.3 mm, which is almost four times bigger than the initial radius. Furthermore, a contour line is plotted to indicate the magnitude of displacement values equal to 1 mm. It is worth to observe that the area affected by unnatural displacements around the tumour is quite extended, indicating that not only the region near the tumour boundary experiences deformations, but there are relevant strains also far from the cancer mass. Moreover, the final volume of the tumour is significantly increased, as it reaches the value of $1737.92\ \text{mm}^3$, while the initial one was $63.24\ \text{mm}^3$, that is more than 27 times smaller, indicating a significant boost in the dimensions of the tumour. To make a comparison with clinical references, we computed some measures of tumour growth that are often used in the biomedical literature. Specifically, we find a volume doubling time (VDT) of about 29.3 days, which is aligned with data from Stensjoen et al. [148] (median VDT: 29.8 days) and from Ellingson et al. [61] (median VDT: 21.1 days). The specific growth rate (SGR), defined as $(\ln 2)/\text{VDT}$, is therefore 2.4%/day, which is also consistent with the mentioned references. However, we remark that such measures are often computed in the clinical literature by assuming an exponential growth law, which might be oversimplified. Another parameter that is sometimes used to quantify brain tumour growth is the average velocity of radial expansion (VRE). In our case, given that

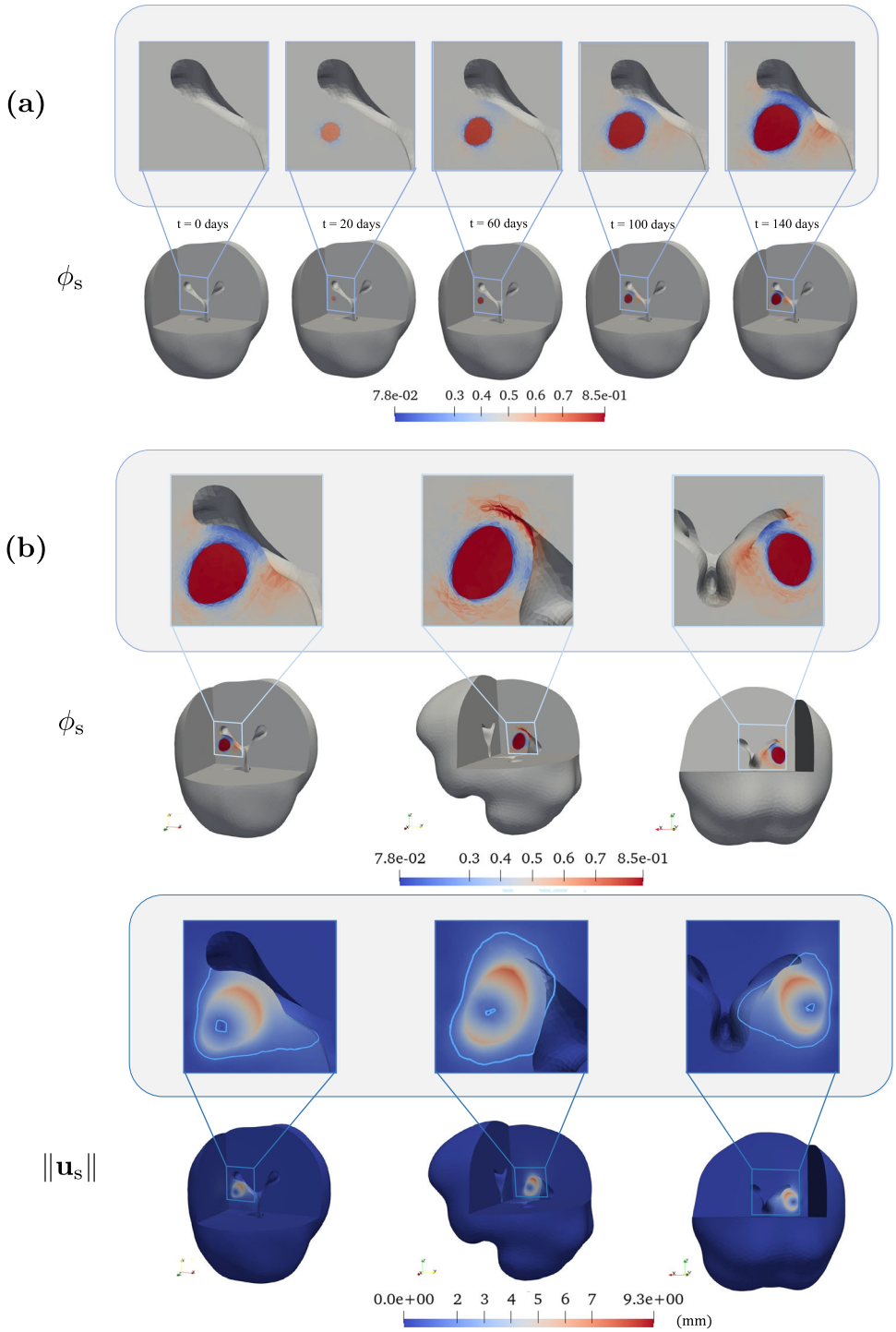

Fig. 3 **a** Temporal evolution of the volumetric fraction of cell population ϕ_s in the brain domain. **b** Comparison between the volumetric fraction of cell population ϕ_s and the displacement magnitude $\|\mathbf{u}_s\|$ after $t = 140$ days of tumour growth in the brain, clipped along three different planes. The insets show a magnification near the ventricles, where the growth phenomenon is primarily happening. (Color figure online)

we have a strongly anisotropic tumour which consistently differs from a sphere, we computed the velocity of expansion along the three axes of the tumour ellipsoid. We find that the VRE along the major axis is approximately $v_{\mathrm{RE}}^{\mathrm{max}} \approx 19.1$ mm/year, whereas the VRE along the intermediate axis is $v_{\mathrm{RE}}^{\mathrm{int}} \approx 12.1$ mm/year and the one along the minor axis is $v_{\mathrm{RE}}^{\mathrm{min}} \approx 10.2$ mm/year. These values are comparable with clinical data [148, 170], even though there is a high variability from patient to patient.

In all these simulations, it is visibly evident that the shape of the tumour is no longer a sphere as it was initially, but the mass has grown along the preferential directions. In order to assess how much anisotropic growth impacts the final shape of the tumour and the size it reaches, we perform the same simulations as before using an isotropic form of the growth

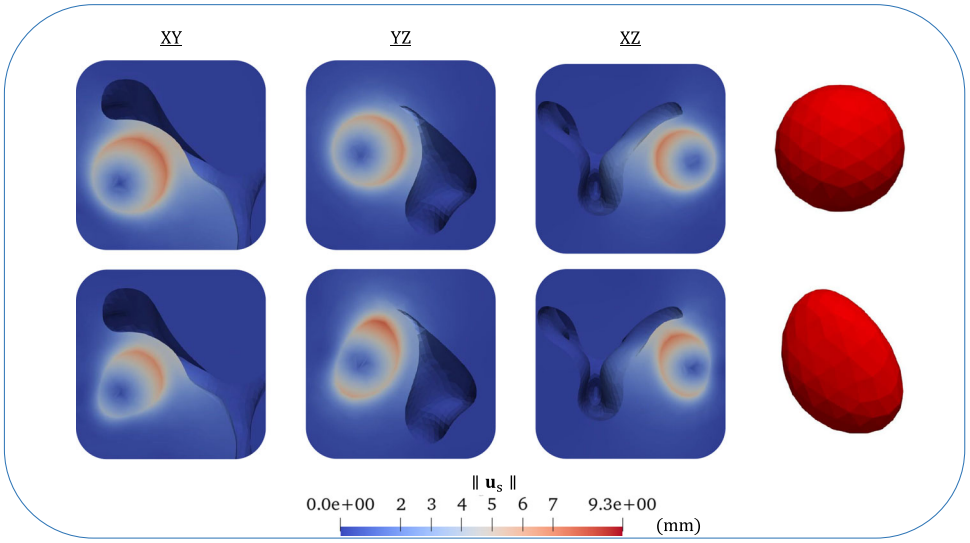

Fig. 4 Comparison between the final magnitude of displacement using *isotropic growth model* (first row) and *anisotropic growth model* (second row), clipped in three different planes at time $t = 140$ days. The last column shows the 3D final shape reached by the tumour at time $t = 140$ days. (Color figure online)

tensor $\mathbb{F}_g = g\mathbb{I}$, while keeping an anisotropic diffusion of the nutrients and permeability tensor (*isotropic growth model*), as done in [23]. In Fig. 4, the magnitude of the displacement at time $t = 140$ days obtained in the latter case is compared to the one obtained with the *anisotropic growth model* proposed in the present work.

It is evident that the hypothesis of an anisotropic growth tensor has a strong impact on the shape that the tumour develops and for this reason it is important to model the presence of preferential growth directions in $\mathbb{F}_g$ to predict the correct tumour expansion. Thus, this work overcomes the limitations of previous mechanical models [23, 116], in which isotropic growth strains were used and the predicted final tumour shapes did not deviate too much from the spherical one. To provide also a quantitative measure of these differences, it is possible to compute a sphericity index, by measuring the lengths of the three representative axes of the tumour at $t = 140$ days in both cases. If we call a the length of the longest axis, b the intermediate one, and c the shortest, we can define the *intercept sphericity* as the cubic root of the ratio between the volume of an ellipsoid having the three diameters a, b, and c and the volume of the circumscribing sphere of diameter a [50, 106, 145]:

$$\psi := \sqrt[3]{bc/a^2}\,. \tag{48}$$

In our cases, for the isotropic growth simulation we obtain $\psi = 0.9834$, whereas we get $\psi = 0.7792$ for the anisotropic case, which means that the latter is definitely more elongated, while the first is more spherical. Furthermore, in order to characterize the anisotropic behaviour of the growth tensor $\mathbb{F}_g$, we introduce two parameters called *linear anisotropy coefficient* (g_ℓ) and *spherical anisotropy coefficient* (g_s), motivated by the definition of c_ℓ and c_s used in evaluating the anisotropy of diffusion in Eq. (33):

$$g_\ell := \frac{g_{\max} - g_{\text{mid}}}{g_{\max} + g_{\text{mid}} + g_{\min}}\,, \quad g_s := \frac{3g_{\min}}{g_{\max} + g_{\text{mid}} + g_{\min}}\,, \tag{49}$$

where $g_{\max} = \max\{g_1, g_2, g_3\}$, $g_{\min} = \min\{g_1, g_2, g_3\}$ and g_{mid} is the remaining one, recalling that g_1, g_2 and g_3 are the eigenvalues of $\mathbb{F}_g$. These coefficients provide insights into the directional preference and overall isotropy of the growth tensor, respectively: a value of $g_\ell \approx 1$ denotes that growth is happening almost entirely along a preferential direction, whereas $g_s \approx 1$ is indicative of isotropic growth. In Fig. 5, the coefficients g_ℓ and g_s across different brain sections are presented at the specific time point of $t = 140$ days.

Regarding the results of the linear anisotropy coefficient, g_ℓ, certain regions within the tumour display values closer to 1, indicating a preference for growth along a specific axis. In contrast, values closer to 0 suggest a more planar or isotropic behaviour. As for the results of g_s, in some regions they generally tend to be closer to zero than to one. This indicates that, in those areas, the deformation within the tumour zone is not isotropic but rather exhibits preferential deformation along specific directions.

As mentioned above, it can be noted that tumour-induced displacement compresses the near brain ventricles: such a clinical issue was pointed out for instance in [5, 147]. The amount of compression can be quantified in terms of volume reduction of the ventricles with respect to the initial configuration. More specifically, we concentrate our analysis on the posterior section of the right lateral ventricle, which is adjacent to the tumour area. This particular region represents approximately half of the total volume of the right lateral ventricle. By tracking its temporal evolution, we observe changes in volume over time. The initial volume, measured computationally, is recorded as 7693.25 mm^3. The evolution in time of the ventricular volume in the region under consideration is

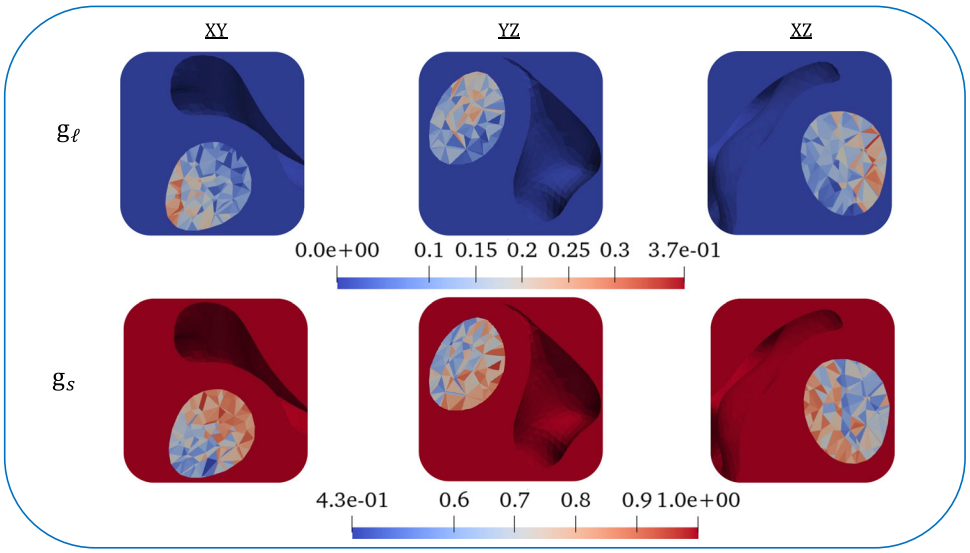

Fig. 5 Visualization of linear (g_ℓ) and spherical (g_s) anisotropy coefficients in three different planes at time $t = 140$ days. (Color figure online)

then reported in Fig. 6, together with a representation of the portion of compressed ventricles. We find that the volume of the portion of the ventricle considered is reduced to a value of 6738.23 mm^3 (corresponding to a decrease of 12.4% of the initial volume) after 140 days of tumour growth, highlighting that a significant compression has occurred in that region. Moreover, we find that the maximum displacement magnitude of the ventricular portion considered amounts at 6.7 mm, which is a notable value, in line with clinical evaluations of ventricular displacement [147, 175]. We remark that in our simulation the edges of the cerebral ventricles never collapse and get into contact. When comparing the compression of the cerebral ventricles between the anisotropic and isotropic simulations, we observe that, with the same tumour volume equal to 1737.92 mm^3, the final volume of the ventricular portion in the isotropic simulation is 6915.51 mm^3. Consequently, in that case the ventricles experience reduced compression. This underscores the significance of incorporating anisotropy into our model, providing a more precise representation of the intricate behaviour of brain tumours within a realistic anatomical environment.

Figure 7 presents the outcomes related to the pressure p, the nutrient concentration c_n and the volumetric solid Cauchy stress $\sigma := -\frac{1}{3}\mathrm{tr}(\mathbb{T}_s)$, where $\mathbb{T}_s = J_s^{-1}\mathbb{P}_s\mathbb{F}_s^T$, at the final time step, depicted in three distinct brain sections.

Looking at the pressure, negative values emerge in the tumour zone, since the fluid is consumed by the cancer mass during uncontrolled cellular growth. Coherently, the concentration of nutrients decreases inside the tumour, where nutrients are consumed by proliferative cells, and near its boundary due to diffusion and transport towards the cancer, while it is maintained at the physiological value of 1 far from the cancer region. We observe that, for the chosen set of parameters, the concentration of nutrients is never above the physiological threshold, i.e. $c_n < 1$. Finally, concerning the volumetric solid Cauchy stress σ, positive values within the tumour region indicate tissue compression therein and suggest the presence of compressive forces acting on the cells. In contrast, negative values surrounding the tumour mass indicate tissue traction, implying the existence of stretching forces in this area. This distribution of stresses highlights the mechanical interactions within the tumour microenvironment and provides insights into the biomechanical behaviour of the surrounding tissue under the influence of the growing tumour. Indeed, the presence of gradients of solid stresses, with tractions near the tumour boundary and compression inside the proliferating mass, is frequently found in experimental analyses [128, 142]. To compare our outcomes with experimental and clinical evidence, first of all we remark that, in our results, $\sigma > 0$ denotes compression, differently from other references in the literature. Given this sign convention, we find that the amount of compressive stress within the tumour area is quantitatively comparable with experimental results on glioma tumour spheroids by Stylianopoulos et al. [153], where compressive stresses range between 5–8 kPa. These values are coherent both with the hydrostatic stress plotted in Fig. 7 and with the hoop stress values of our model, which inside the tumour area vary between 1–9 kPa of compressive stress. A range of 1.3–13.3 kPa is pointed out by Stylianopoulos et al. in another work about tumour spheroids [152], though in that case the results are not brain-specific. Moreover, by using a poroelastic model with experimentally informed parameters for tumour spheroids, Fraldi and Carotenuto [67] found compressive stress values that are comparable with ours. Instead, measurements of stresses in murine brain tumours by Seano and coworkers [142] display compressive stress values of the order of 10^{-1} kPa. This discrepancy might be due to the material model

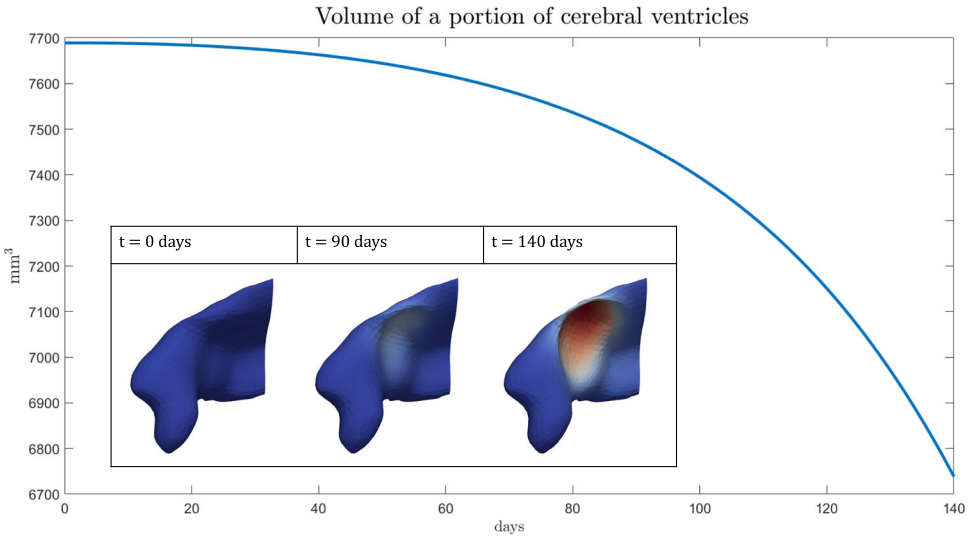

Fig. 6 Volume of a portion of cerebral ventricles over time. In the bottom left, a graphical representation of the cerebral ventricles at three different time instants ($t = 0,\ 90,\ 140$ days) is shown. (Color figure online)

chosen and to the difference in stiffness between the tumour and the host tissue, as pointed out in [116]. Furthermore, we observe that relatively high compression values of the volumetric solid Cauchy stress σ can also be found at the interface between the healthy tissue and the ventricles, in the presence of high deformations. Indeed, at this boundary, while the normal component of the stress is null, the tangential/hoop component of the stress may be significantly elevated. In this case, given the forthcoming contact scenario, it will be important to model contact boundary conditions for a thorough analysis of the stress distribution in this region, a consideration that will be addressed in future research. Concerning the fluid pressure, our results display a decrease inside the tumour region due to the cells consuming fluid therein, in accordance with other works using mixture models [75, 76]. However, other references [67, 152] report an increase in the interstitial fluid pressure within the tumour. The discrepancy is due to the fact that these models also account for possible fluid inflow due to vessel leakage and osmotic pressure differences, as well as for outflow due to lymphatic drainage. We did not consider such effects in our model, although a Starling-like law could be easily incorporated and would be interesting to investigate.

Finally, we present the findings concerning the impact of tumour growth on DTI data. As the tumour expands and displaces the surrounding tissue, it alters the natural arrangement of fibre tracts, resulting in noticeable modifications in the preferred directions of diffusion and fluid motion. To quantify this effect, we employ a scalar parameter known as *fractional anisotropy* (FA), which is calculated based on the descending order eigenvalues of the diffusion tensor (λ_1, λ_2, and λ_3) as

$$\mathrm{FA} := \sqrt{\frac{1}{2}\frac{(\lambda_1-\lambda_2)^2+(\lambda_2-\lambda_3)^2+(\lambda_1-\lambda_3)^2}{\lambda_1^2+\lambda_2^2+\lambda_3^2}}. \tag{50}$$

A fractional anisotropy value of 0 indicates an isotropic environment where the eigenvalues are all equal to each other, resulting in a diffusion ellipsoid resembling a sphere with no preferred direction. Conversely, a fractional anisotropy value of 1 identifies the presence of a single preferential direction, limiting diffusion to happen exclusively along one of the eigenvectors. To assess the alteration of the diffusion tensor over time due to tumour-induced deformation, we compute the fractional anisotropy of the diffusion tensor $\mathbb{D}$ at the final time point ($t = 140$ days) of the simulation where no therapies were included and subtract it from the fractional anisotropy of the initial time diffusion tensor $\mathbb{D}^0$, i.e. we evaluate $\Delta\mathrm{FA}_{\mathbb{D}} := \mathrm{FA}_{\mathbb{D}} - \mathrm{FA}_{\mathbb{D}^0}$. Similarly, we compute the variation of fractional anisotropy for the tensor $\mathbb{D}_{\mathrm{NFW}}$ at $t = 140$ days, which takes into account the motion influenced by the fibres. This variation is denoted as $\Delta\mathrm{FA}_{\mathbb{D}_{\mathrm{NFW}}} := \mathrm{FA}_{\mathbb{D}_{\mathrm{NFW}}} - \mathrm{FA}_{\mathbb{D}^0_{\mathrm{NFW}}}$. Such an index is comparable to the so-called Free Water Eliminated Fractional Anisotropy (FWE–FA) reported in certain medical studies [27]. The findings derived from computing differences between initial and final data on each cell of the mesh are presented in Fig. 8.

For what concerns the non-free water diffusion tensor $\mathbb{D}_{\mathrm{NFW}}$, there is a notable increase in diffusive anisotropy in the region surrounding the expanding tumour. The variations in fractional anisotropy are not uniform around the tumour area, revealing distinct zones that experience significant changes in anisotropy while others maintain their initial preferred directions. In particular, we notice that the FA associated to $\mathbb{D}_{\mathrm{NFW}}$ within the tumour bulk mostly remains constant. This is due to the fact that we modify the tensor $\mathbb{D}_{\mathrm{NFW}}$ by means of the solid deformation, which is greater around the tumour domain. As a consequence, the most relevant alterations in anisotropy are observed in the surroundings, where displacements attain higher values and the

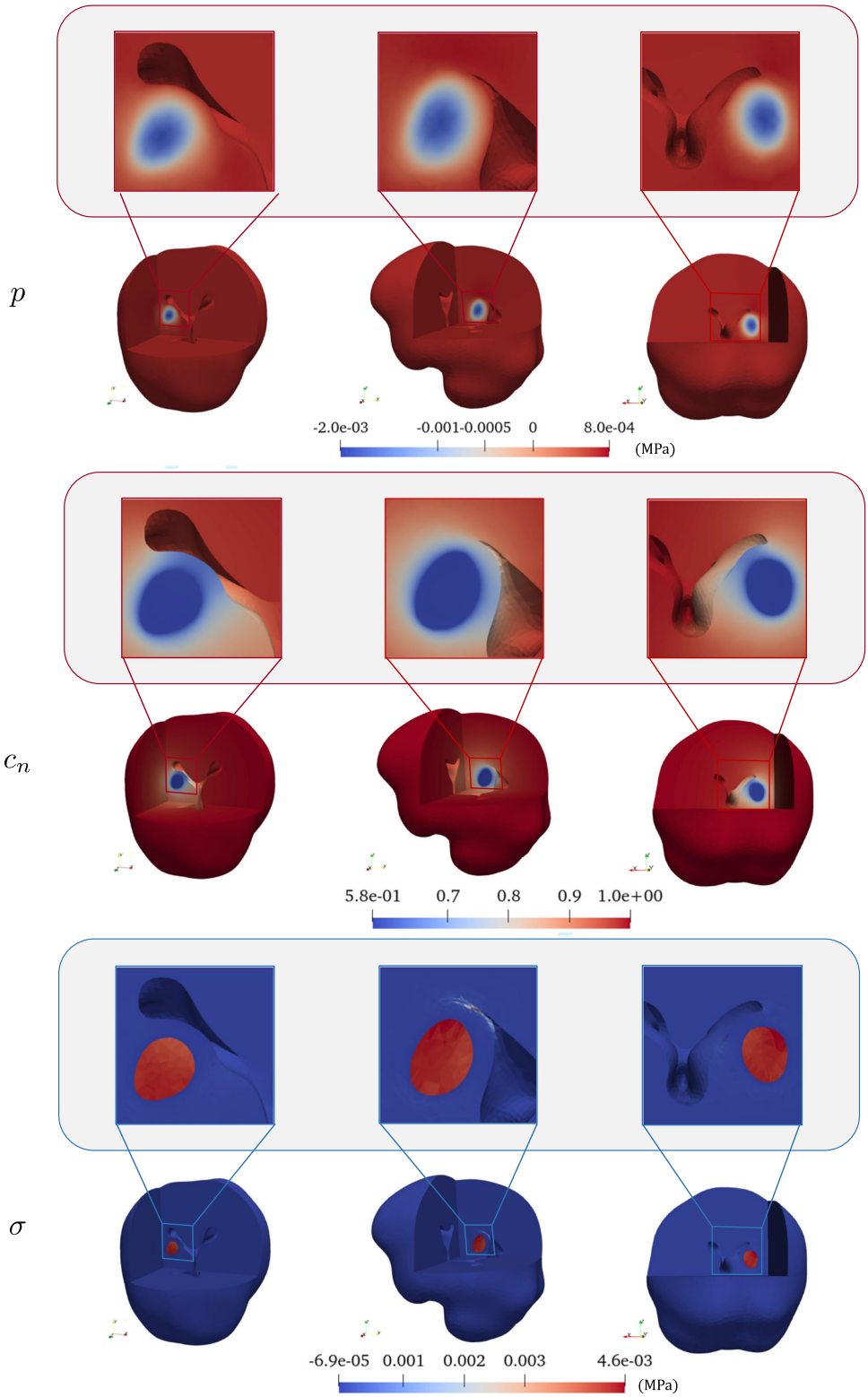

Fig. 7 Comparison between the pressure p, the concentration of nutrients c_n and $\sigma := -\frac{1}{3}\mathrm{tr}(\mathbb{T}_s)$ after $t = 140$ days of tumour growth in the brain, clipped along three different planes. The insets show a magnification near the ventricles, where the growth phenomenon is primarily happening. (Color figure online)

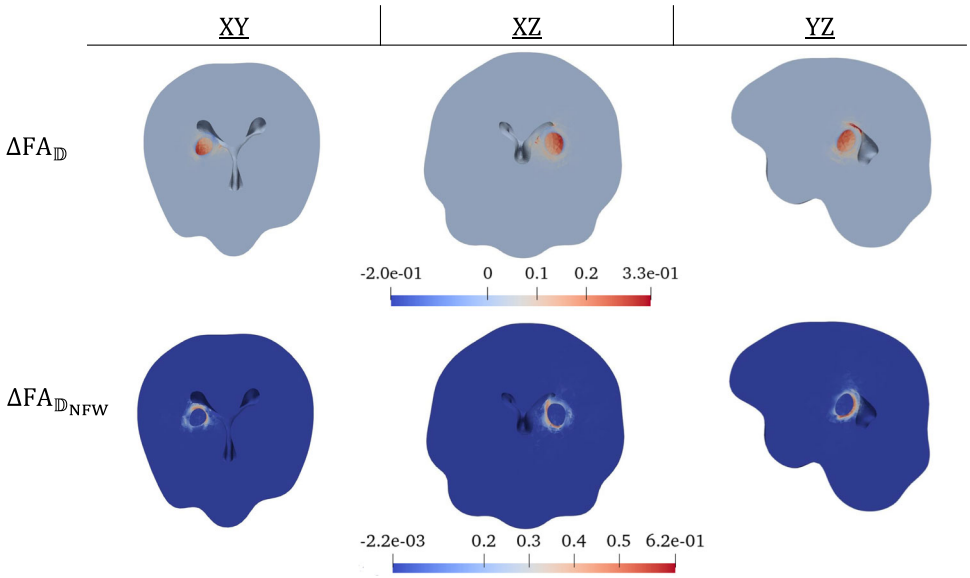

Fig. 8 Variation in fractional anisotropy (FA) over 140 days of tumour growth, comparing the diffusion tensor ($\mathbb{D}$) and its non-free water component ($\mathbb{D}_{NFW}$). (Color figure online)

cancer mass dislocates the white matter fibres. The reconstruction of DTI data inside the tumour is a non-trivial problem, given that such data often appear to be altered by the cancerous mass in patients, even at the first scan. Therefore, the modelling of anisotropy changes inside the tumour may require further research efforts [158], also accounting for damage of fibres and reconstruction algorithms. On the other hand, as far as the diffusion tensor $\mathbb{D}$ is concerned, it can be observed that, in the regions near the ventricles, there is a decrease in fractional anisotropy, which is reflected in negative values of $\Delta FA_{\mathbb{D}}$. This is because the presence of more fluid results in a higher weighting of the isotropic component of the tensor, recalling Eq. (26). On the contrary, in the area within the tumour, the increase in ϕ_s results in a greater importance attributed to the non-free water component of $\mathbb{D}$, leading to observed increases in FA with respect to initial DTI data, where more fluid was present.

4.2 Simulations including radiotherapy and chemotherapy

After having studied the effect of anisotropic growth and its impact on cerebral ventricles, we incorporate radiotherapy and chemotherapy into our mathematical model. Such a capability represents a relevant feature of our framework, as it may allow to evaluate treatment efficacy by simulating the effects of therapies on tumour progression. This might be of help in understanding how the tumour responds to treatments and provide insights into potential therapeutic strategies, which are often very challenging for brain tumours. Secondly, the model may assist in optimising treatment protocols by simulating different schedules, dosages, and drug combinations, aiding in personalised treatment planning.

First of all, we conducted a simulation by incorporating the first protocol presented in Sect. 2.1.1 and defined by Eqs. (9a)–(9b), using the parameters discussed in Sect. 3.2, and we refer to this case as *standard therapy*. Secondly, we performed a simulation adding to the model the prolonged effects of the chemotherapeutic drug in treating the tumour, as modelled in Eq. (11), applying the parameters discussed in Sect. 3.2. We denote this second scenario as *standard therapy with decay*. Finally, in a third simulation, we increased the parameters of the therapies, by using $R_{\text{eff}} = 0.07128\ \text{day}^{-1}$ and $k_{C1} = 0.043\ \text{day}^{-1}$, always preserving the decay. For what concerns the radiotherapy coefficient, this is equivalent to an approximate increase of 11% from the initial value, which remains within the clinically acceptable range [139], whereas the chemotherapy coefficient exhibits a significantly higher increase, specifically 485%. This could be interpreted as the use of a more powerful drug or a combination of different drugs to control tumour growth, as done in some medical trials. In this third scenario, the parameters k_{C2} and k_{C3} are instead chosen to achieve the same response in terms of chemotherapy-induced cell death rate at the beginning of each cycle, taking into account the prolonged effect of the drug. The aim of the second and third cycles is therefore to restore the already high lethal effect on cancer cells achieved in the first cycle. Specifically, the required values are $k_{C2} = 0.035\ \text{day}^{-1}$ and $k_{C3} = 0.034\ \text{day}^{-1}$. We refer to the latter case as *enhanced RT and CHT with decay*. Graphs illustrating the temporal evolution of $k_R(t)$ and $k_C(t)$ for the three different scenarios are reported in Fig. 9.

The results obtained in all these three cases with therapies are compared in Fig. 10 with the case where the tumour is not treated. In particular, Fig. 10a displays the variation of the average value of Γ_s, which represents a measure of the growth rate of the tumour mass. In Fig. 10b we show the

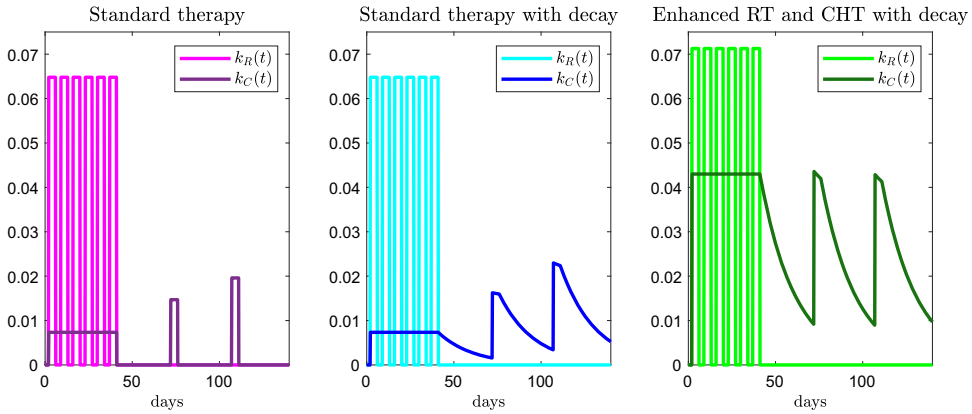

Fig. 9 The graphs show a comparisons among the variations of $k_R(t)$ and $k_C(t)$ over time in the three therapeutic protocols considered in the paper. (Color figure online)

evolution of the average value of the fraction of solid phase ϕ_s, whereas Fig. 10c reports the changes in tumour volume over time. From these results, it is possible to observe how the tumour responds differently by changing the therapeutic approach. As expected, the case without therapy leads to the fastest and greatest growth, while the introduction of therapies is reflected by the reduction in volume and growth rate. In particular, an enhancement in therapies may allow to significantly contain the progression of the cancer. This could be highly beneficial from a medical perspective, as it suggests that an intensified treatment strategy has the potential to significantly impact tumour growth and potentially improve patient outcomes. Hence, these results demonstrate that, by integrating diverse parameters and variables, including drug concentration, tumour growth rate, and drug sensitivity, the model can effectively simulate and predict the outcomes of different drug treatments. Simulations like these could therefore be useful to tune the dosage of drugs or the intervals of administration of therapies, for instance, in order to minimise the growth of the cancer.

Finally, in Fig. 11, the volume fraction of the solid phase is plotted at the initial time instant and at $t = 140$ days, in order to compare the initial size of the tumour with the shape reached at the end of the simulations performed both without introducing any therapy and including a treatment. It can be observed that the case without therapy obviously leads to the biggest tumour mass after about five months of growth, whereas the introduction of therapeutic protocols is able to contain the expansion of the cancer. Such an outcome is especially important when growth near delicate cerebral structures like the ventricles is studied, given that a proper therapeutic treatment may be helpful to avoid unnatural ventricular compression. To quantify the response of the tumour to therapies in the first 39 days, where RT and CHT are simultaneously performed, we computed the percent variation in the tumour principal diameters with respect to the initial size, following the RECIST criteria for solid tumours [131]. First of all, we notice that, in the case without therapy, the major axis of the tumour increases by 92%, while the increase along the minor one amounts at 32%, with an average along the three directions of about 56% increase in diameter. Instead we find that, for the case of standard therapy, the major axis of the tumour increases by 54% and the minor axis by 3%, with an average of about 24% increase. The case of standard therapy with decay improves the outcomes, but only slightly. In these cases, even if growth is slowed down, the tumour is still classified as progressive according to medical standards [131]. Instead, when we consider enhanced RT and CHT with decay, the percent increase of the tumour major axis amounts at 16%, whereas a -1% reduction is observed along the minor axis, with an average in the three directions of about only 6% increase. In the latter case, resorting to the RECIST criteria, the tumour can be classified as stable and not progressive anymore [131], falling within the typical response window also highlighted in other models of brain tumour treatment [138, 139].

5 Conclusions

Brain tumours are among the most difficult to treat with current therapeutic protocols, due to their aggressiveness and to a significant resistance to therapies. In addition, the impact of a growing cancer mass inside the brain may be particularly harmful for the patient, since it may deform and compress delicate structures like the ventricles. As a consequence of damage affecting healthy areas of the brain, neurological issues can emerge and negatively affect the prognosis of patients affected by such cancers. Based on these observations, in this paper we have proposed a mathematical model and computational framework that feature three main novelties compared with previous works. First of all, we explicitly accounted for the presence of ventricles in the cerebral geometry, so that a precise quantification of unnatural ventricular compression following tumour growth can be performed. In particular, the deformation and volume variation of the ventricles can be studied thanks to the mechanical nature of the model, which is able to evaluate

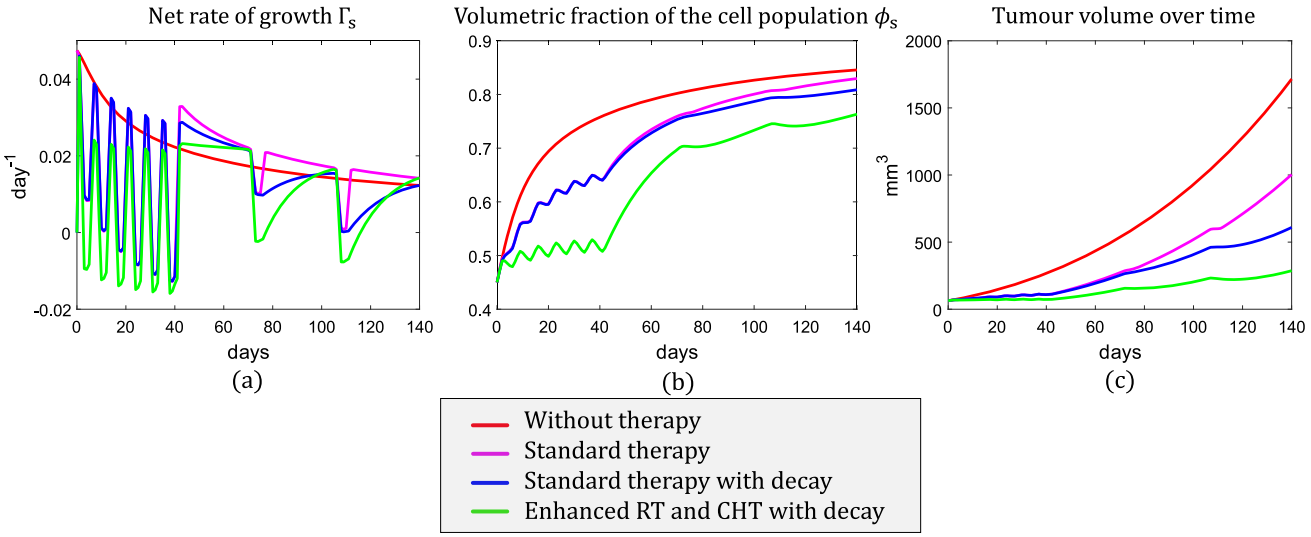

Fig. 10 In the graphs, a comparison between the variations of Γ_s (**a**), ϕ_s (**b**) and the volume of the tumour (**c**) over time is shown. The red line represents the scenario without any therapy, while the magenta line corresponds to the scenario including the standard therapy. Additionally, we included the blue line to illustrate the standard therapy with the consideration of a time decay of the drugs. Lastly, the green line represents the scenario with enhanced radiotherapy and chemotherapy. (Color figure online)

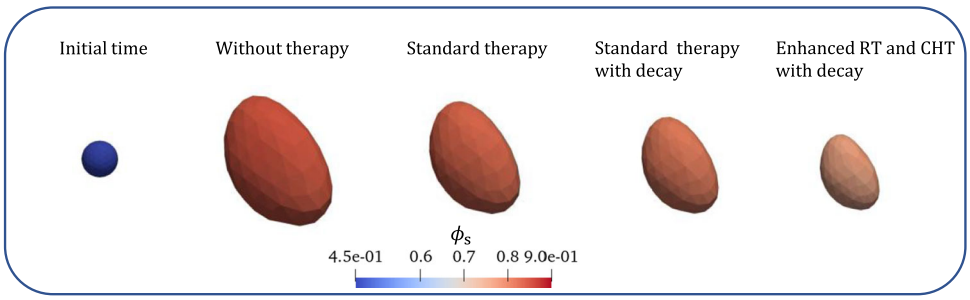

Fig. 11 Volumetric fraction of the cell population, plotted at the initial time and after different simulations both with and without therapeutic protocols, at time $t = 140$ days. (Color figure online)

tumour-induced strains as well as fluid motion. Indeed, we consider the brain as a mixture of a nonlinear elastic solid phase and an ideal fluid phase, within the framework of mixture theory. Moreover, we employ a sharp interface model to simulate solid localized brain tumours, which are responsible for the higher mechanical deformations of the surrounding tissue. This choice, however, does not allow to capture the behaviour of infiltrating cancers, which are characterized by small clusters of tumour cells and show extensive growth and dissemination far from the primary cancer mass, as considered for instance in [89, 110, 126]. Secondly, we consider growth distortions as anisotropic, to overcome the simplified assumption of isotropic growth which is frequently made in the literature. Such a choice is justified by the presence of oriented fibre structures in the brain, i.e. the white matter tracts, along which tumour cells may preferentially move and grow. This anisotropy creates irregular and heterogeneous growth patterns, with tumours becoming highly non-spherical during their proliferation. In addition, we consider also diffusion and fluid motion as anisotropic phenomena affecting the tumour and its environment, so that the proposed framework embeds three anisotropic components: the diffusion tensor $\mathbb{D}$, the permeability tensor $\mathbb{K}$, and the growth-related distortion tensor $\mathbb{F}_g$. As an additional capability of the model, all these tensors are computationally reconstructed from medical imaging data, with a specific focus on free-water diffusion, related to the free liquid in the brain, and non-free-water diffusion, characterised by preferential motion along the fibres. Thirdly, the model includes cancer treatment via chemotherapy and radiotherapy, and it can be fruitfully employed to simulate different therapeutic strategies aimed at slowing down tumour growth.

Our numerical results confirm the validity of the proposed model as a proof-of-concept for simulating fully anisotropic brain tumour progression, as well as therapeutic protocols and ventricular compression. In particular, we find that an initially spherical tumour can become highly elongated during growth and may exert a significant compression on the nearby ventricles, increasing the risk of neurological damage due to excessive intracranial pressure and fluid flow obstruc-

tion. Clear differences are highlighted between the case of isotropic and anisotropic growth, suggesting that the role of brain fibre structures is fundamental in driving the evolution of the tumour shape and size. A large region around the tumour zone is also found to be affected by unnatural displacements, which might be harmful for patients. Finally, we have shown that the model is capable of reproducing therapeutic strategies, pointing out methods to slow down cancer progression. Furthermore, the model can be readily adapted to simulate different therapies and schedules, such as concomitant treatment with different chemoterapies [25] or ultra-fractionated radiotherapy [28, 29], allowing the exploration of potentially effective, tailored protocols.

In conclusion, we have proposed a framework that can represent a first step towards a realistic simulation of anisotropic, patient-specific, mechanically motivated brain tumour growth, together with therapeutic treatment. Regarding possible future developments, it would be important to model the contact of ventricle edges when they touch due to deformations caused by cancer. Such a situation, which is never reached in our simulations, would require an appropriate treatment by means of contact mechanics. Furthermore, we aim to integrate a voxel-wise estimation of free water in the brain to establish a more appropriate and spatially-dependent initial value for ϕ_ℓ^0 and, consequently, for ϕ_s^0. Possible heterogeneity between grey and white matter from a mechanical viewpoint could also be incorporated in the proposed framework, especially if tumours of comparable stiffness to the healthy tissue are considered. We also note that in our model we have neglected fluid exchange between the tissue and the vasculature, assuming that the only source of fluid is cell death within the domain and fluid flow at the tissue-ventricle boundary. This assumption is more appropriate for representing avascular or poorly vascularised tumours. Therefore, future models should focus on the description of the vasculature and lymphatic system (either from a homogenised point of view [67, 121] or by implementing a 3D-1D coupling between the tissue and the vasculature [31, 41]) in order to properly describe the vascular growth phase of the tumour. Moreover, we are aware that our model for therapies is a simplification of the much more complex biological phenomenon, but this approach allows us to simulate the ongoing effects of therapies without taking into account the intricate biological processes initiated by the drug, or eventually radiation, in the context of a computationally sophisticated model. In this respect, clinical data could be used to test, validate and possibly modify the model about therapies, establishing the values of RT and CHT parameters, and explicitly including TMZ pharmacodynamics to better represent the late cell death after treatment. In addition, the integration of optimal control theories presents an intriguing avenue to enhance our research. Future perspectives could be focused on exploring this promising approach for developing optimal timing and dosing strategies for chemotherapeutic drugs, addressing a prominent issue of medical significance, as exemplified in [46]. Finally, the model should be adapted to simulate surgical resection before chemoradiation therapies, which represents a challenging modelling task and has not been targeted in the present work.

A Weak formulation of the Lagrangian model

The weak formulation of the Lagrangian model is derived in the following. The weak form is first written in each domain Ω_t^* and Ω_h^* separately and then it is extended to the whole domain $\Omega^* = \Omega_t^* \cup \Omega_h^*$. First of all, it is necessary to define the test functions spaces that meet the Dirichlet conditions imposed on the external boundary for c_n (39c) and on ventricles boundary for p (40b), recalling that p and c_n are continuous functions over Ω^*:

$$H^1_{0,\partial\Omega^*_{\text{out}}}(\Omega^*) := \left\{ q \in H^1(\Omega^*) \colon q = 0 \text{ on } \partial\Omega^*_{\text{out}} \right\},$$
$$H^1_{0,\partial\Omega^*_{\text{v}}}(\Omega^*) := \left\{ q \in H^1(\Omega^*) \colon q = 0 \text{ on } \partial\Omega^*_{\text{v}} \right\}.$$

Furthermore, we establish the vector test functions space that meets the Dirichlet conditions we impose on the external boundary for the continuous vector function $\mathbf{u}_s$ (39a):

$$\boldsymbol{H}^1_{0,\partial\Omega^*_{\text{out}}}(\Omega^*) := \left\{ \boldsymbol{q} \in \boldsymbol{H}^1(\Omega^*) \colon \boldsymbol{q} = \mathbf{0} \text{ on } \partial\Omega^*_{\text{out}} \right\}.$$

Then, starting from Eq. (14), we multiply each side by a test function $q_t \in H^1_{0,\partial\Omega^*_{\text{v}}}(\Omega^*)$ and we integrate the whole equation over the Lagrangian tumour domain Ω_t^*:

$$\int_{\Omega_t^*} \dot{J}_s q_t \, dV^* = \int_{\Omega_t^*} \text{Div}\left[\frac{\mathbb{K}^*}{\mu} \text{Grad}\, p \right] q_t \, dV^*. \tag{A.1}$$

Integrating by parts the second order derivatives, we obtain

$$\int_{\Omega_t^*} \dot{J}_s q_t \, dV^* = -\int_{\Omega_t^*} \text{Grad}\, q_t \cdot \frac{\mathbb{K}^*}{\mu} \text{Grad}\, p \, dV^* + \\ + \int_{\partial\Omega_t^*} q_t \frac{\mathbb{K}^*}{\mu} \text{Grad}\, p \cdot \mathbf{N} d\Sigma^*. \tag{A.2}$$

In the healthy domain we take as test function $q_h \in H^1_{0,\partial\Omega^*_{\text{v}}}(\Omega^*)$ and we find

$$\int_{\Omega_h^*} \dot{J}_s q_h \, dV^* = -\int_{\Omega_h^*} \text{Grad}\, q_h \cdot \frac{\mathbb{K}^*}{\mu} \text{Grad}\, p \, dV^* + \\ + \int_{\partial\Omega_t^*} q_h \frac{\mathbb{K}^*}{\mu} \text{Grad}\, p \cdot \mathbf{N} d\Sigma^* +$$

$$+\int_{\partial\Omega^*_{\text{out}}} q_{\text{h}}\frac{\mathbb{K}^*}{\mu}\,\text{Grad}\,p\cdot\mathbf{N}d\Sigma^*+$$
$$+\int_{\partial\Omega^*_{\text{v}}} q_{\text{h}}\frac{\mathbb{K}^*}{\mu}\,\text{Grad}\,p\cdot\mathbf{N}d\Sigma^*\,. \tag{A.3}$$

The test function q_{h} is required to vanish on the boundary $\partial\Omega^*_{\text{v}}$ because it belongs to $H^1_{0,\partial\Omega^*_{\text{v}}}(\Omega^*)$. Furthermore, the second-last integral vanishes due to the boundary condition (39b). Summing up the equations in the healthy and tumour domain and taking $q\in H^1_{0,\partial\Omega^*_{\text{v}}}(\Omega^*)$ we have

$$\int_{\Omega^*}\dot{J}_{\text{s}}q\,dV^*=-\int_{\Omega^*}\text{Grad}\,q\cdot\frac{\mathbb{K}^*}{\mu}\,\text{Grad}\,p\,dV^*+$$
$$-\int_{\partial\Omega^*_{\text{t}}}[\![q\frac{\mathbb{K}^*}{\mu}\,\text{Grad}\,p]\!]\cdot\mathbf{N}d\Sigma^*\,, \tag{A.4}$$

where $[\![\cdot]\!]$ denotes the jump across the interface. Since the test function q belongs to $H^1_{0,\partial\Omega^*_{\text{v}}}(\Omega^*)$ and for this reason it is continuous inside the domain, remembering interface condition (38b) we finally have

$$\int_{\Omega^*}\dot{J}_{\text{s}}q\,dV^*=-\int_{\Omega^*}\text{Grad}\,q\cdot\frac{\mathbb{K}^*}{\mu}\,\text{Grad}\,p\,dV^*\,, \tag{A.5}$$

for all test functions $q\in H^1_{0,\partial\Omega^*_{\text{v}}}(\Omega^*)$.

For what concerns the momentum balance, we multiply Eq. (13) by a vector test function $\boldsymbol{q}_{\text{t}}\in\boldsymbol{H}^1_{0,\partial\Omega^*_{\text{out}}}(\Omega^*)$ and then we integrate over the tumour reference domain, obtaining

$$\int_{\Omega^*_{\text{t}}}\text{Div}\left[-J_{\text{s}}p\mathbb{F}_{\text{s}}^{-\text{T}}+\mathbb{P}_{\text{s}}\right]\cdot\boldsymbol{q}_{\text{t}}\,dV^*=0\,. \tag{A.6}$$

Using tensor integration by parts, we get

$$-\int_{\Omega^*_{\text{t}}}\left(-J_{\text{s}}p\mathbb{F}_{\text{s}}^{-\text{T}}+\mathbb{P}_{\text{s}}\right):\text{Grad}\,\boldsymbol{q}_{\text{t}}\,dV^*+$$
$$+\int_{\partial\Omega^*_{\text{t}}}\left(-J_{\text{s}}p\mathbb{F}_{\text{s}}^{-\text{T}}+\mathbb{P}_{\text{s}}\right)\mathbf{N}\cdot\boldsymbol{q}_{\text{t}}\,d\Sigma^*=0\,, \tag{A.7}$$

where : denotes the double contraction between tensors. If we do the same in the healthy domain using as test function $\boldsymbol{q}_{\text{h}}\in\boldsymbol{H}^1_{0,\partial\Omega^*_{\text{out}}}(\Omega^*)$, we obtain

$$-\int_{\Omega^*_{\text{h}}}\left(-J_{\text{s}}p\mathbb{F}_{\text{s}}^{-\text{T}}+\mathbb{P}_{\text{s}}\right):\text{Grad}\,\boldsymbol{q}_{\text{h}}\,dV^*+$$
$$+\int_{\partial\Omega^*_{\text{t}}}\left(-J_{\text{s}}p\mathbb{F}_{\text{s}}^{-\text{T}}+\mathbb{P}_{\text{s}}\right)\mathbf{N}\cdot\boldsymbol{q}_{\text{h}}\,d\Sigma^*+$$
$$+\int_{\partial\Omega^*_{\text{out}}}\left(-J_{\text{s}}p\mathbb{F}_{\text{s}}^{-\text{T}}+\mathbb{P}_{\text{s}}\right)\mathbf{N}\cdot\boldsymbol{q}_{\text{h}}\,d\Sigma^*+$$
$$+\int_{\partial\Omega^*_{\text{v}}}\left(-J_{\text{s}}p\mathbb{F}_{\text{s}}^{-\text{T}}+\mathbb{P}_{\text{s}}\right)\mathbf{N}\cdot\boldsymbol{q}_{\text{h}}\,d\Sigma^*=0\,. \tag{A.8}$$

If we remember that $\boldsymbol{q}_{\text{h}}\in\boldsymbol{H}^1_{0,\partial\Omega^*_{\text{out}}}(\Omega^*)$, the second last integral vanishes. Using condition (40a), the last summand of the last integral is equal to zero, and therefore we have

$$-\int_{\Omega^*_{\text{h}}}\left(-J_{\text{s}}p\mathbb{F}_{\text{s}}^{-\text{T}}+\mathbb{P}_{\text{s}}\right):\text{Grad}\,\boldsymbol{q}_{\text{h}}\,dV^*+$$
$$+\int_{\partial\Omega^*_{\text{t}}}\left(-J_{\text{s}}p\mathbb{F}_{\text{s}}^{-\text{T}}+\mathbb{P}_{\text{s}}\right)\mathbf{N}\cdot\boldsymbol{q}_{\text{h}}\,d\Sigma^*+$$
$$-\int_{\partial\Omega^*_{\text{v}}}J_{\text{s}}p\mathbb{F}_{\text{s}}^{-\text{T}}\mathbf{N}\cdot\boldsymbol{q}_{\text{h}}\,d\Sigma^*=0\,. \tag{A.9}$$

Summing up Eqs. (A.7) and (A.9) and taking $\boldsymbol{q}\in\boldsymbol{H}^1_{0,\partial\Omega^*_{\text{out}}}(\Omega^*)$, the weak formulation on the whole domain is

$$-\int_{\Omega^*}\left(-J_{\text{s}}p\mathbb{F}_{\text{s}}^{-\text{T}}+\mathbb{P}_{\text{s}}\right):\text{Grad}\,\boldsymbol{q}\,dV^*+$$
$$-\int_{\partial\Omega^*_{\text{t}}}[\![\left(-J_{\text{s}}p\mathbb{F}_{\text{s}}^{-\text{T}}+\mathbb{P}_{\text{s}}\right)\mathbf{N}\cdot\boldsymbol{q}]\!]d\Sigma^*+$$
$$-\int_{\partial\Omega^*_{\text{v}}}J_{\text{s}}p\mathbb{F}_{\text{s}}^{-\text{T}}\mathbf{N}\cdot\boldsymbol{q}\,d\Sigma^*=0\,. \tag{A.10}$$

Recalling that the displacement is taken continuous in all directions (38a), the areas deform in the same way at the interface. The relation $d\boldsymbol{\Sigma}=J_{\text{s}}\mathbb{F}_{\text{s}}^{-\text{T}}d\boldsymbol{\Sigma}^*$, where $d\boldsymbol{\Sigma}=\mathbf{n}d\Sigma$ represents the infinitesimal element of area in spatial coordinates and $d\boldsymbol{\Sigma}^*=\mathbf{N}d\Sigma^*$ denotes the infinitesimal element of area in material coordinates, implies $[\![J_{\text{s}}\mathbb{F}_{\text{s}}^{-\text{T}}\mathbf{N}]\!]|_{\partial\Omega^*_{\text{t}}}=\mathbf{0}$. Looking at this condition and at the interface conditions (38c) and (38d) and recalling that $\boldsymbol{q}\in\boldsymbol{H}^1_{0,\partial\Omega^*_{\text{out}}}(\Omega^*)$, the jump in Eq. (A.10) vanishes. Furthermore, the pressure p on $\partial\Omega^*_{\text{v}}$ is fixed by (40b) and it assumes the constant value p_{v}. At the end we are left with

$$-\int_{\Omega^*}\left(-J_{\text{s}}p\mathbb{F}_{\text{s}}^{-\text{T}}+\mathbb{P}_{\text{s}}\right):\text{Grad}\,\boldsymbol{q}\,dV^*+$$
$$-\int_{\partial\Omega^*_{\text{v}}}J_{\text{s}}p_{\text{v}}\mathbb{F}_{\text{s}}^{-\text{T}}\mathbf{N}\cdot\boldsymbol{q}_{\text{t}}\,d\Sigma^*=0\,. \tag{A.11}$$

The variational problems in Eqs. (A.5) and (A.11) are nonlinear and coupled: in view of the numerical implementation, it is convenient to rewrite them into a single nonlinear variational problem by summing them. If we do that, we obtain a variational problem for the displacement and the pressure:

$$\int_{\Omega^*}\dot{J}_{\text{s}}q\,dV^*+\int_{\Omega^*}\text{Grad}\,q\cdot\frac{\mathbb{K}^*}{\mu}\,\text{Grad}\,p\,dV^*+$$
$$-\int_{\Omega^*}\left(-J_{\text{s}}p\mathbb{F}_{\text{s}}^{-\text{T}}+\mathbb{P}_{\text{s}}\right):\text{Grad}\,\boldsymbol{q}\,dV^*+$$
$$-\int_{\partial\Omega^*_{\text{v}}}J_{\text{s}}p_{\text{v}}\mathbb{F}_{\text{s}}^{-\text{T}}\mathbf{N}\cdot\boldsymbol{q}_{\text{t}}\,d\Sigma^*=0\,. \tag{A.12}$$

We need then a weak formulation for the equation of the nutrients. In order to derive it, we multiply Eq. (5) by a test function $q_\mathrm{t} \in H^1_{0,\partial\Omega^*_\mathrm{out}}(\Omega^*)$ and we integrate by parts, obtaining

$$\begin{aligned}
&\int_{\Omega^*_\mathrm{t}} \left(J_\mathrm{s}\phi_\ell \dot{c}_n - \frac{\mathbb{K}^*}{\mu}\,\mathrm{Grad}\; p \cdot \mathrm{Grad}\; c_n \right) q_\mathrm{t}\, dV^* + \\
&+ \int_{\Omega^*_\mathrm{t}} \phi_\ell\, \mathrm{Grad}\, q_\mathrm{t} \cdot \mathbb{D}^*\, \mathrm{Grad}\, c_n\, dV^* + \\
&- \int_{\partial\Omega^*_\mathrm{t}} q_\mathrm{t}\phi_\ell \mathbb{D}^*\, \mathrm{Grad}\, c_n \cdot \mathbf{N} d\Sigma^* = \int_{\Omega^*_\mathrm{t}} J_\mathrm{s} G_n q_\mathrm{t}\, dV^* .
\end{aligned} \tag{A.13}$$

We follow the same approach in the healthy domain:

$$\begin{aligned}
&\int_{\Omega^*_\mathrm{h}} \left(J_\mathrm{s}\phi_\ell \dot{c}_n - \frac{\mathbb{K}^*}{\mu}\,\mathrm{Grad}\; p \cdot \mathrm{Grad}\; c_n \right) q_\mathrm{h}\, dV^* + \\
&+ \int_{\Omega^*_\mathrm{h}} \phi_\ell\, \mathrm{Grad}\, q_\mathrm{h} \cdot \mathbb{D}^*\, \mathrm{Grad}\, c_n\, dV^* + \\
&- \int_{\partial\Omega^*_\mathrm{t}} q_\mathrm{h}\phi_\ell \mathbb{D}^*\, \mathrm{Grad}\, c_n \cdot \mathbf{N} d\Sigma^* + \\
&- \int_{\partial\Omega^*_\mathrm{out}} q_\mathrm{h}\phi_\ell \mathbb{D}^*\, \mathrm{Grad}\, c_n \cdot \mathbf{N} d\Sigma^* + \\
&- \int_{\partial\Omega^*_\mathrm{v}} q_\mathrm{h}\phi_\ell \mathbb{D}^*\, \mathrm{Grad}\, c_n \cdot \mathbf{N} d\Sigma^* = \int_{\Omega^*_\mathrm{h}} J_\mathrm{s} G_n q_\mathrm{h}\, dV^* .
\end{aligned} \tag{A.14}$$

For what concerns the last two surface integrals on the l.h.s., they vanish using the fact that $q_\mathrm{h} \in H^1_{0,\partial\Omega^*_\mathrm{out}}(\Omega^*)$ and the boundary condition (40c) on $\partial\Omega^*_\mathrm{v}$. Then we sum Eqs. (A.13) and (A.14) and, recalling the interface condition (38f) and the fact that the test function $q \in H^1_{0,\partial\Omega^*_\mathrm{out}}(\Omega^*)$ is continuous along $\partial\Omega^*_\mathrm{t}$, we finally have

$$\begin{aligned}
&\int_{\Omega^*} \left(J_\mathrm{s}\phi_\ell \dot{c}_n - \frac{\mathbb{K}^*}{\mu}\,\mathrm{Grad}\; p \cdot \mathrm{Grad}\; c_n \right) q\, dV^* + \\
&+ \int_{\Omega^*} \phi_\ell\, \mathrm{Grad}\, q \cdot \mathbb{D}^*\, \mathrm{Grad}\, c_n\, dV^* = \\
&= \int_{\Omega^*} J_\mathrm{s} G_n q\, dV^* .
\end{aligned} \tag{A.15}$$

We remark that, given the pressure p and the displacement $\mathbf{u}_\mathrm{s}$ obtained by solving (A.5) and (A.11), Eq. (A.15) represents a linear variational problem to be solved for the unknown c_n.

B Image acquisition

In this Appendix, we provide details on the process by which information regarding the shape and tissues of the patient's brain, as well as the most probable direction of the white matter fibers, was derived from MRI and DTI. Imaging data were acquired at the Fondazione IRCCS Istituto Neurologico Besta (Milan, Italy). The patient signed a written consent to the MRI and DTI tests in the context of normal clinical practice, including clinical research. The patient was not submitted to any specific procedure different from normal clinical practice and the collected patient data was anonymized and de-identified prior to analysis. Anonymization was performed by the neuroradiology unit of the Besta Neurological Institute, independently from the researchers involved in the paper.

To visualize the MRI data of the patient's brain, we use the open-source software *3D Slicer* [1, 65]. Since we are interested in identifying fluid regions, we focus on T1-weighted images, where fluid appears dark and tissue appears white. The initial step involves image segmentation, dividing it into distinct and homogeneous regions, emphasizing the areas of interest to facilitate analysis. We then choose a task, leveraging provided atlases (images from various patients that are already labeled) to identify the ventricular region within the new image and assign an appropriate label. In our case, we select the MRI Human Brain task and perform segmentation through *3D Slicer*'s automatic segmentation. Additionally, smoothing can be applied to the generated maps. The next step involves extracting the brain external surface and ventricle surface from the segmented map using *Vmtk* (Vascular Modeling ToolKit) [165]. Finally, using *Tetgen* [80, 164], a program capable of generating tetrahedral meshes for any 3D polyhedral domain, the mesh is constructed. The external surface represents the brain's outer surface, while the inner surface corresponds to the brain-ventricle boundary. We observe that we construct a tumour-conformal mesh to distinctly separate the healthy from the tumour domain. The latter is considered as a sphere with a radius of 2.5 mm. *Tetgen* is again employed to refine the tetrahedral mesh within a spherical area centered on the tumour. In Fig. 12, the constructed mesh is shown.

Now it is necessary to incorporate information from Diffusion Tensor Imaging (DTI) into the mesh. Each cell of the 3D mesh requires assignment of a symmetric 3×3 tensor, specifically the symmetric tensor denoted as $\mathbb{D}^0_{\mathrm{NFW}}$, containing water diffusion values along the principal spatial directions. In this specific case, the initial data consists of medical images that only contain the non-free water information, already available from the files provided by the medical professionals. Our task involves processing the medical images and subsequently transferring the values to the three-dimensional mesh. In detail, we generate six meshes, each dedicated to one independent component of the tensor. Since perfect alignment is required for transferring data from images to meshes, *image registration* becomes necessary. This involves realigning the images as accurately as

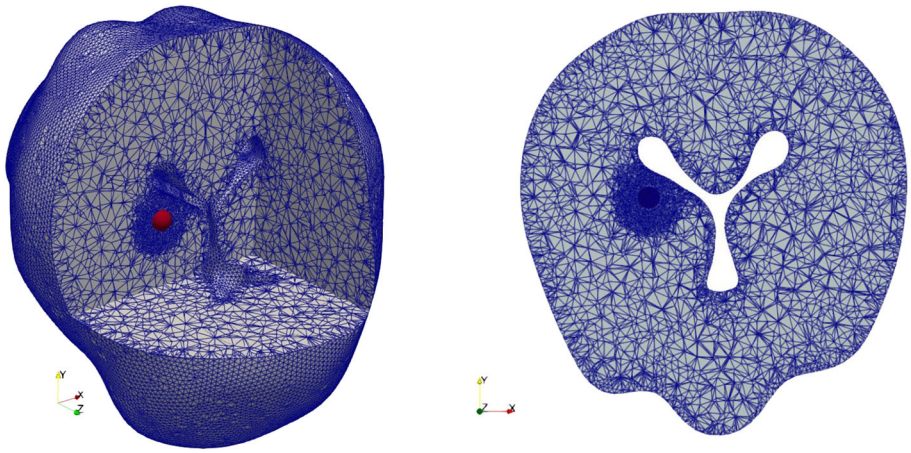

Fig. 12 Computational brain mesh and refinement, with tumour region highlighted in red. (Color figure online)

possible with our reference map. For this purpose, we use *FSL* (FMRIB Software Library) [66, 95] and select FLIRT, the FMRIB's linear registration tool specifically designed for images from the same patient, as in our scenario. With all diffusion tensor components aligned with the maps segmented from magnetic resonances and, consequently, with the tetrahedral mesh, we can proceed to assign diffusion values to the cells of the mesh. This task can be accomplished using specific commands in *Vmtk* [165].

Acknowledgements This work has been partially supported by the Italian Ministry of University and Research through the *Research Project of National Interest* PRIN2020 n. 2020F3NCPX, PRIN2022-PNRR n. P2022Z7ZAJ (CUP: E53D23018070001), and PRIN2022 n. 2022YFTS7N (CUP: 53D23002240006). The authors are members of the National Group of Mathematical Physics (GNFM) of the Italian Institute for High Mathematics (INdAM). GL acknowledges the support of GNFM–INdAM through the project *Progetto Giovani 2023* CUP: E53C22001930001. Computational resources were provided by HPC@POLITO (https://hpc.polito.it/). The neuroimaging data used in this study were gently provided by Dr. Francesco Acerbi and Dr. Alberto Bizzi (Istituto Neurologico Carlo Besta, Milan, Italy). We are indebted to Aymeric Stamm and Pasquale Ciarletta for their valuable collaboration in the development of the procedures for MRI and DTI image analysis.

Funding Open access funding provided by Politecnico di Torino within the CRUI-CARE Agreement.

References

1. 3D Slicer image computing platform. https://www.slicer.org/
2. Agosti A, Cattaneo C, Giverso C, Ambrosi D, Ciarletta P (2018) A computational framework for the personalized clinical treatment of glioblastoma multiforme. ZAMM J Appl Math Mech/Zeitschrift f ü r Angewandte Mathematik und Mechanik 98(12):2307–2327
3. Agosti A, Ciarletta P, Garcke H, Hinze M (2020) Learning patient-specific parameters for a diffuse interface glioblastoma model from neuroimaging data. Math Methods Appl Sci 43(15):8945–8979
4. Agosti A, Giverso C, Faggiano E, Stamm A, Ciarletta P (2018) A personalized mathematical tool for neuro-oncology: a clinical case study. Int J Non-Linear Mech 107:170–81
5. Ahmed A, UlHaq MU, Mustansar Z, Shaukat A, Margetts L (2021) How growing tumour impacts intracranial pressure and deformation mechanics of brain. R Soc Open Sci 8(9):210165
6. Albeck MJ, Børgesen SE, Gjerris F, Schmidt JF, Sørensen PS (1991) Intracranial pressure and cerebrospinal fluid outflow conductance in healthy subjects. J Neurosurg 74(4):597–600
7. Alentorn A, Hoang-Xuan K, Mikkelsen T (2006) Presenting signs and symptoms in brain tumors. Handb Clin Neurol 134:19–26
8. Alexander AL, Lee JE, Lazar M, Field AS (2007) Diffusion tensor imaging of the brain. Neurother Adv Neuroimaging/Neuroethics 4(3):316–329
9. Alfonso JCL, Talkenberger K, Seifert M, Klink B, Hawkins-Daarud A, Swanson KR, Hatzikirou H, Deutsch A (2017) The biology and mathematical modelling of glioma invasion: a review. J R Soc Interface 14(136):20170490
10. Alnaes M, Blechta J, Hake J, Johansson A, Kehlet B, Logg A, Richardson C, Ring J, Rognes ME, Wells GN (2015) The FEniCS project version 1.5. Arch Numer Software 3:100
11. Ambrosi D, Ben Amar M, Cyron C, DeSimone A, Goriely A, Humphrey J, Kuhl E (2019) Growth and remodelling of living tissues: perspectives, challenges and opportunities. J R Soc Interface 16:20190233
12. Ambrosi D, Preziosi L (2009) Cell adhesion mechanisms and stress relaxation in the mechanics of tumours. Biomech Model Mechanobiol 8:397–413
13. Ambrosi D, Preziosi L, Vitale G (2009) The insight of mixtures theory for growth and remodeling. Zeitschrift f ü r angewandte Mathematik und Physik 61:177–191
14. Ambrosi D, Mollica F (2002) On the mechanics of a growing tumor. Int J Eng Sci 40(12):1297–1316

15. Ambrosi D, Mollica F (2004) The role of stress in the growth of a multicell spheroid. J Math Biol 48:477–499
16. Ambrosi D, Preziosi L (2002) On the closure of mass balance models for tumor growth. Math Models Methods Appl Sci 12(05):737–754
17. Andresen M, Juhler M (2014) Intracranial pressure following complete removal of a small demarcated brain tumor: a model for normal intracranial pressure in humans: Clinical article. J Neurosurg JNS 121(4):797–801
18. Angeli S, Emblem KE, Due-Tonnessen P, Stylianopoulos T (2018) Towards patient-specific modeling of brain tumor growth and formation of secondary nodes guided by DTI-MRI. NeuroImage Clin 20:664–673
19. Angeli S, Stylianopoulos T (2016) Biphasic modeling of brain tumor biomechanics and response to radiation treatment. J Biomech 49(9):1524–1531
20. Asgari M, de Zelicourt D, Kurtcuoglu V (2016) Glymphatic solute transport does not require bulk flow. Sci Rep 6:38635
21. Athesian G, Weiss J (2010) Anisotropic hydraulic permeability under finite deformation. J Biomech Eng 132:111004
22. Balbi V, Trotta A, Destrade M, Ní Annaidh A (2019) Poynting effect of brain matter in torsion. Soft Matter 15(25):5147–5153
23. Ballatore F, Lucci G, Borio A, Giverso C (2023) An imaging-informed mechanical framework to provide a quantitative description of brain tumour growth and the subsequent deformation of white matter tracts. In: Bretti G, Natalini R, Palumbo P, Preziosi L (eds) Mathematical models and computer simulations for biomedical applications. Springer SEMA SIMAI Springer Series, vol. 33. Springer, Cham
24. Barazzuol L, Burnet N, Jena R, Jones B, Jefferies S, Kirkby N (2010) A mathematical model of brain tumour response to radiotherapy and chemotherapy considering radiobiological aspects. J Theor Biol 262:553–565
25. Barrié M et al (2005) Temozolomide in combination with BCNU before and after radiotherapy in patients with inoperable newly diagnosed glioblastoma multiforme. Ann Oncol 16(7):1177–1184
26. Basser PJ (1992) Interstitial pressure, volume, and flow during infusion into brain tissue. Microvasc Res 44(2):143–165
27. Bauer CE, Zachariou V, Maillard P, Caprihan A, Gold BT (2022) Multi-compartment diffusion magnetic resonance imaging models link tract-related characteristics with working memory performance in healthy older adults. Front Aging Neurosci 14:995425
28. Beauchesne P, Quillien V, Faure G, Bernier V, Noel G, Quetin P, Gorlia T, Carnin C, Pedeux R (2016) A concurrent ultrafractionated radiation therapy and temozolomide treatment: a promising therapy for newly diagnosed, inoperable glioblastoma. Int J Cancer 138(6):1538–1544
29. Beauchesne P et al (2010) Prolonged survival for patients with newly diagnosed, inoperable glioblastoma with 3-times daily ultrafractionated radiation therapy. Neuro-Oncol 12(6):595–602
30. Beltzig L, Stratenwerth B, Kaina B (2021) Accumulation of temozolomide-induced apoptosis, senescence and dna damage by metronomic dose schedule: a proof-of-principle study with glioblastoma cells. Cancers 13:24
31. Berrone S, Giverso C, Grappein D, Preziosi L, Scialò S (2023) An optimization based 3D–1D coupling strategy for tissue perfusion and chemical transport during tumor-induced angiogenesis. Comput Math Appl 151:252–270
32. Bogdanska M, Bodnar M, Belmonte-Beitia J, Murek M, Schucht P, Beck J, Perez-Garcia V (2017) A mathematical model of low grade gliomas treated with temozolomide and its therapeutical implications. Math Biosci 288:1–13
33. Bondiau P-Y, Konukoglu E, Clatz O, Delingette H, Frenay M, Paquis P (2011) Biocomputing: numerical simulation of glioblastoma growth and comparison with conventional irradiation margins. Physica Med 27(2):103–108
34. Böttger K, Hatzikirou H, Chauviere A, Deutsch A (2012) Investigation of the migration/proliferation dichotomy and its impact on avascular glioma invasion. Math Model Natl Phenomena 7(1):105–135
35. Branco J, Ferreira J, de Oliveira P (2014) Mathematical modeling of efficient protocols to control glioma growth. Math Biosci 255:83–90
36. Bruehlmeier M, Roelcke U, Bläuenstein P, Missimer J, Schubiger P, Locher J, Pellikka R, Ametamey S (2003) Measurement of the extracellular space in brain tumors using 76Br-bromide and PET. J Nucl Med 44:1210–8
37. Budday S, Ovaert TC, Holzapfel GA, Steinmann P, Kuhl E (2020) Fifty shades of brain: a review on the mechanical testing and modeling of brain tissue. Arch Comput Methods Eng 27(4):1187–1230
38. Budday S et al (2017) Mechanical characterization of human brain tissue. Acta Biomater 48:319–340
39. Budday S, Nay R, de Rooij R, Steinmann P, Wyrobek T, Ovaert T, Kuhl E (2015) Mechanical properties of gray and white matter brain tissue by indentation. J Mech Behav Biomed Mater 46:318–330
40. Byrne H, Preziosi L (2004) Modelling solid tumour growth using the theory of mixtures. Math Med Biol 20:341–66
41. Cattaneo L, Zunino P (2014) Computational models for fluid exchange between microcirculation and tissue interstitium. Netw Heterogeneous Media 9(1):135–159
42. Chatelain C, Balois T, Ciarletta P, Ben Amar M (2011) Emergence of microstructural patterns in skin cancer: a phase separation analysis in a binary mixture. New J Phys 13(11):115013
43. Chauffert B, Feuvret L, Bonnetain F, Taillandier L et al (2014) Randomized phase II trial of irinotecan and bevacizumab as neoadjuvant and adjuvant to temozolomide-based chemoradiation compared with temozolomide-chemoradiation for unresectable glioblastoma: final results of the TEMAVIR study from ANOCEF. Ann Oncol 25:1442–1447
44. Chauvet D, Imbault M, Capelle L, Demené C, Mossad M, Karachi C, Boch A-L, Gennisson J-L, Tanter M (2016) In vivo measurement of brain tumor elasticity using intraoperative shear wave elastography. Ultraschall in der Medizin 37:584–90
45. Clatz O, Sermesant M, Bondiau P-Y, Delingette H, Warfield SK, Malandain G, Ayache N (2005) Realistic simulation of the 3-D growth of brain tumors in MR images coupling diffusion with biomechanical deformation. IEEE Trans Med Imaging 24:1334–1346
46. Colli P, Gomez H, Lorenzo G, Marinoschi G, Reali A, Rocca E (2021) Optimal control of cytotoxic and antiangiogenic therapies on prostate cancer growth. Math Models Methods Appl Sci 31(07):1419–1468
47. Colombo MC, Giverso C, Faggiano E, Boffano C, Acerbi F, Ciarletta P (2015) Towards the personalized treatment of glioblastoma: integrating patient-specific clinical data in a continuous mechanical model. PLoS ONE 10(7):1–23
48. Conte M, Dzierma Y, Knobe S, Surulescu C (2023) Mathematical modeling of glioma invasion and therapy approaches via kinetic theory of active particles. Math Models Methods Appl Sci 33(05):1009–1051
49. Conte M, Surulescu C (2021) Mathematical modeling of glioma invasion: acid- and vasculature mediated go-or-grow dichotomy and the influence of tissue anisotropy. Appl Math Comput 407:126305
50. Cruz-Matías I, Ayala D, Hiller D, Gutsch S, Zacharias M, Estradé S, Peiró F (2019) Sphericity and roundness computation for particles using the extreme vertices model. J Comput Sci 30:28–40
51. DeAngelis L (2001) Brain tumors. N Engl J Med 344(2):114–123

52. Destrade M, Gilchrist M, Murphyj J, Rashid B, Saccomandi G (2015) Extreme softness of brain matter in simple shear. Int J Non-Linear Mech 75:54–58
53. Di Stefano S, Giammarini A, Giverso C, Grillo A (2022) An elasto-plastic biphasic model of the compression of multicellular aggregates: the influence of fluid on stress and deformation. ZAMP - Zeitschrift f ü r angewandte Mathematik und Physik 73:79
54. Di Stefano S, Carfagna M, Knodel MM, Hashlamoun K, Federico S, Grillo A (2019) Anelastic Reorganisation of Fibre-Reinforced Biological Tissues. Comput Vis Sci 20(3–6):95–109
55. DiCarlo A, Quiligotti S (2002) Growth and balance. Mech Res Commun 29(6):449–456
56. de Rooij R, Kuhl E (2016) Constitutive modeling of brain tissue: current perspectives. Appl Mech Rev 68(1):1–16
57. Ehlers W, Eipper G (1999) Finite elastic deformations in liquid-saturated and empty porous solids. Transp Porous Media 34:179–191
58. Ehlers W, Morrison Rehm M, Schröder P, Stöhr D, Wagner A (2022) Multiphasic modelling and computation of metastatic lung-cancer cell proliferation and atrophy in brain tissue based on experimental data. Biomech Model Mechanobiol 21(1):277–315
59. Ehlers W, Wagner A (2015) Multi-component modelling of human brain tissue: a contribution to the constitutive and computational description of deformation, flow and diffusion processes with application to the invasive drug-delivery problem. Comput Methods Biomech Biomed Eng 18(8):861–879
60. Elazab A, Anter AM, Bai H, Hu Q, Hussain Z, Ni D, Wang T, Lei B (2019) An optimized generic cerebral tumor growth modeling framework by coupling biomechanical and diffusive models with treatment effects. Appl Soft Comput 80(C):617–627
61. Ellingson B, Nguyen H, Lai A, Nechifor R, Zaw O, Pope W, Yong W, Nghiemphu P, Liau L, Cloughesy T (2016) Contrast-enhancing tumor growth dynamics of preoperative, treatment-naive human glioblastoma. Cancer 122:1718–1727
62. Engwer C, Hillen T, Knappitsch M, Surulescu C (2014) Glioma follow white matter tracts: a multiscale DTI-based model. J Math Biol 71:551–582
63. Engwer C, Hunt A, Surulescu C (2015) Effective equations for anisotropic glioma spread with proliferation: a multiscale approach and comparisons with previous settings. Math Med Biol 33:435–459
64. Esmaeili M, Stensjøen AL, Berntsen EM, Solheim O, Reinertsen I (2018) The direction of tumour growth in glioblastoma patients. Sci Rep 8:1
65. Fedorov A et al (2012) 3D slicer as an image computing platform for the quantitative imaging network. Magn Reson Imaging 30:1323–41
66. FMRIB Software Library. https://fsl.fmrib.ox.ac.uk/fsl/fslwiki
67. Fraldi M, Carotenuto A (2019) Cells competition in tumor growth poroelasticity. J Mech Phys Solids 112:345–367
68. Fresnais M, Turcan S, Theile D, Ungermann J, Abou Zeed Y, Lindner JR, Breitkopf M, Burhenne J, Haefeli WE, Longuespée R (2022) Approaching sites of action of temozolomide for pharmacological and clinical studies in glioblastoma. Biomedicines 10:1
69. Frieboes H, Lowengrub J, Wise S, Zheng X, Macklin P, Bearer E, Cristini V (2007) Computer simulation of glioma growth and morphology. Neuroimage 37:S59–S70
70. Friedman H, Kerby T, Calvert H (2000) Temozolomide and treatment of malignant glioma. Clin Cancer Res 6(7):2585–2597
71. Gamburg ES, Regine WF, Patchell RA, Strottmann JM, Mohiuddin M, Young AB (2000) The prognostic significance of midline shift at presentation on survival in patients with glioblastoma multiforme. Int J Radiat Oncol Biol Phys 48(5):1359–1362
72. Garcia J, Smith J (2009) A biphasic hyperelastic model for the analysis of fluid and mass transport in brain tissue. Ann Biomed Eng 37(2):375–386
73. Gerlee P, Anderson A (2007) An evolutionary hybrid cellular automaton model of solid tumour growth. J Theor Biol 246(4):583–603
74. Giese A, Kluwe L, Laube B, Meissner H, Berens ME, Westphal M (1996) Migration of human glioma cells on myelin. Neurosurgery 38:755–764
75. Giverso C, Preziosi L (2019) Influence of the mechanical properties of the necrotic core on the growth and remodelling of tumour spheroids. Int J Non-Linear Mech 108:20–32
76. Giverso C, Scianna M, Grillo A (2015) Growing avascular tumours as elasto-plastic bodies by the theory of evolving natural configurations. Mech Res Commun 68:31–39
77. Goriely A (2017) The mathematics and mechanics of biological growth. Springer
78. Green M, Bilston LE, Sinkus R (2008) In vivo brain viscoelastic properties measured by magnetic resonance elastography. NMR Biomed 21:755–64
79. Grillo A, Federico S, Wittum G (2012) Growth, mass transfer, and remodeling in fiber-reinforced, multi-constituent materials. Int J Non-Linear Mech 47(2):388–401
80. Hang S (2015) TetGen, a delaunay-based quality tetrahedral mesh generator. ACM Trans Math Softw 41(2):1–36
81. Harkos C, Svensson SF, Emblem KE, Stylianopoulos T (2022) Inducing biomechanical heterogeneity in brain tumor modeling by MR elastography: effects on tumor growth, vascular density and delivery of therapeutics. Cancers 14(4):884
82. Hatzikirou H, Basanta D, Simon M, Schaller K, Deutsch A (2012) "Go or Grow": The key to the emergence of invasion in tumour progression? Math Medi Biol 29:49–65
83. He Y, Kaina B (2019) Are there thresholds in glioblastoma cell death responses triggered by temozolomide? Int J Mol Sci 20(7):1562
84. Hervey-Jumper SL, Berger MS (2020) Introduction: surgical management of eloquent area tumors. Neurosurgery 87(6):1076–1077
85. Hoehme S et al (2010) Prediction and validation of cell alignment along microvessels as order principle to restore tissue architecture in liver regeneration. Proc Natl Acad Sci 107(23):10371–10376
86. Hogea C, Davatzikos C, Biros G (2008) An image-driven parameter estimation problem for a reaction-diffusion glioma growth model with mass effects. J Math Biol 56:793–825
87. Holdsworth C, Corwin D, Stewart R, Rockne R, Trister A, Swanson K, Phillips M (2012) Adaptive IMRT using a multiobjective evolutionary algorithm integrated with a diffusion-invasion model of glioblastoma. Phys Med Biol 57(24):8271
88. Holmes M, Mow V (1990) The nonlinear characteristics of soft gels and hydrated connective tissues in ultrafiltration. J Biomech Eng 23(11):1145–1156
89. Hormuth D, Al Feghali K, Elliott A, Yankeelov T, Chung C (2021) Image-based personalization of computational models for predicting response of high-grade glioma to chemoradiation. Sci Rep 11:8520
90. Hormuth D II, Fahrat M, Christenson C, Curl B, Quarles C, Chung C, Yankeelov T (2022) Opportunities for improving brain cancer treatment outcomes through imaging-based mathematical modeling of the delivery of radiotherapy and immunotherapy. Adv Drug Deliv Rev 187:114367
91. Hormuth D II, Weis J, Barnes S, Miga M, Quaranta V, Yankeelov T (2017) A mechanically coupled reaction-diffusion model that incorporates intra-tumoural heterogeneity to predict in vivo glioma growth. J R Soc Interface 14:20161010

92. Hunt A, Surulescu C (2016) A Multiscale Modeling Approach to Glioma Invasion with Therapy. Vietnam J Math 45:221–240
93. Iarosz K, Borges F, Batista A, Baptista M, Siqueira R, Viana R, Lopes S (2015) Mathematical model of brain tumour with glia-neuron interactions and chemotherapy treatment. J Theor Biol 368:113–121
94. Jbabdi S, Mandonnet E, Duffau H, Capelle L, Swanson KR, Pélégrini-Issac M, Guillevin R, Benali H (2005) Simulation of anisotropic growth of low-grade gliomas using diffusion tensor imaging. Magn Reson Med 54(3):616–624
95. Jenkinson M, Beckmann C, Behrens T, Woolrich M, Smith S (2012) FSL. NeuroImage 62(2):782–790
96. Jin B-J, Smith A, Verkman A (2016) Spatial model of convective solute transport in brain extracellular space does not support a "glymphatic" mechanism. J Gen Physiol 148:489–501
97. Jui S-L, Zhang S, Xiong W, Yu F, Fu M, Wang D (2016) Brain MRI tumor segmentation with 3D intracranial structure deformation features. IEEE Intell Syst 31(2):66–76
98. Kalli M, Voutouri C, Minia A, Pliaka V, Fotis C, Alexopoulos LG, Stylianopoulos T (2019) Mechanical compression regulates brain cancer cell migration through MEK1/Erk1 pathway activation and GDF15 expression. Front Oncol 9:992
99. Kansal A, Torquato S, Harsh G, Chiocca E, Deisboeck T (2000) Simulated brain tumor growth dynamics using a three-dimensional cellular automaton. J Theor Biol 203:367–82
100. Kaufman L, Brangwynne C, Kasza K, Filippidi E, Gordon V, Deisboeck T, Weitz D (2005) Glioma expansion in collagen I matrices: analyzing collagen concentration-dependent growth and motility patterns. Biophys J 89(1):635–650
101. Khain E, Katakowski M, Hopkins S, Szalad A, Zheng X, Jiang F, Chopp M (2011) Collective behavior of brain tumor cells: the role of hypoxia. Phys Rev E 83(3):031920
102. Khajanchi S, Nieto J (2021) Spatiotemporal dynamics of a glioma immune interaction model. Sci Rep 11:22385
103. Khan E, Lane M, Sagher O (2017) Eloquent: history of a word's adoption into the neurosurgical lexicon. J Neurosurg 127(6):1461–1466
104. Kim MM, Umemura Y, Leung D (2018) Bevacizumab and glioblastoma: past, present, and future directions. Cancer J 24(4):180–186
105. Kono K, Inoue Y, Nakayama K, Shakudo M, Morino M, Ohata K, Wakasa K, Yamada R (2001) The role of diffusion-weighted imaging in patients with brain tumors. Am J Neuroradiol 22(6):1081–1088
106. Krumbein WC (1941) Measurement and geological significance of shape and roundness of sedimentary particles. J Sediment Res 11(2):64–72
107. Lattanzi AM, Yin X, Hrenya CM (2019) A fully-developed boundary condition for the random walk particle tracking method. Int J Heat Mass Transf 131:604–610
108. Le Bihan D, Iima M (2015) Diffusion magnetic resonance imaging: what water tells us about biological tissues. PLoS Biol 13(7):1–13
109. Lipkova J, Menze B, Wiestler B, Koumoutsakos P, Lowengrub J (2022) Modeling glioma progression, mass-effect, and intracranial pressure in patient anatomy. J R Soc Interface 19:20210922
110. Lipková J et al (2019) Personalized radiotherapy design for glioblastoma: integrating mathematical tumor models, multimodal scans, and bayesian inference. IEEE Trans Med Imaging 38(8):1875–1884
111. Liu J, Hormuth D II, Davis T, Yang J, McKenna M, Jarrett A, Enderling H, Brock A, Yankeelov T (2021) A mathematical model of low grade gliomas treated with temozolomide and its therapeutical implications. Integr Biol 13(7):167–183
112. Löber-Handwerker R, Döring K, Bock C, Rohde V, Malinova V (2022) Defining the impact of adjuvant treatment on the prognosis of patients with inoperable glioblastoma undergoing biopsy-only: Does the survival benefit outweigh the treatment effort? Neurosurg Rev 45:2339–2347
113. Logg A, Mardal K-A, Wells G (2012) Automated solution of differential equations by the Finite Element Method. Springer
114. Lou E et al (2013) Phase II trial of upfront bevacizumab and temozolomide for unresectable or multifocal glioblastoma. Cancer Med 2(2):185–195
115. Lubarda VA (2004) Constitutive theories based on the multiplicative decomposition of deformation gradient: Thermoelasticity, elastoplasticity, and biomechanics. Appl Mech Rev 57(2):95–108
116. Lucci G, Agosti A, Ciarletta P, Giverso C (2022) Coupling solid and fluid stresses with brain tumour growth and white matter tract deformations in a neuroimaging-informed model. Biomech Model Mechanobiol 21:1483–1509
117. MacLaurin J, Chapman J, Jones G, Roose T (2012) The buckling of capillaries in solid tumours. Proc R Soc A 468:4123–4145
118. Madhusoodanan S, Ting M, Farah T, Ugur U (2015) Psychiatric aspects of brain tumors: a review. World J Psychiatry 5:273–285
119. Mansury Y, Kimura M, Lobo J, Deisboeck T (2002) Emerging patterns in tumor systems: simulating the dynamics of multicellular clusters with an agent-based spatial agglomeration model. J Theor Biol 219:343–370
120. Mascheroni P, Carfagna M, Grillo A, Boso D, Schrefler B (2018) An avascular tumor growth model based on porous media mechanics and evolving natural states. Math Mech Solids 23(4):686–712
121. Mascheroni P, Penta R, Merodio J (2023) The impact of vascular volume fraction and compressibility of the interstitial matrix on vascularised poroelastic tissues. Biomech Model Mechanobiol 22(6):1901–1917
122. Mascheroni P, Stigliano C, Carfagna M, Boso D, Preziosi L, Decuzzi P, Schrefler B (2016) Predicting the growth of glioblastoma multiforme spheroids using a multiphase porous media model. Biomech Model Mechanobiol 15:1215–1228
123. Mihai L, Budday S, Holzapfel G, Kuhl E, Goriely A (2017) A family of hyperelastic models for human brain tissue. J Mech Phys Solids 106:60–79
124. Miroshnikova Y et al (2016) Tissue mechanics promote IDH1-dependent HIF1 α -tenascin C feedback to regulate glioblastoma aggression. Nat Cell Biol 18:1336–45
125. Motz CT, Kabat V, Saxena T, Bellamkonda RV, Zhu C (2021) Neuromechanobiology: an expanding field driven by the force of greater focus. Adv Healthcare Mater 19(10):e2100102
126. Neal ML et al (2013) Discriminating survival outcomes in patients with glioblastoma using a simulation-based, patient-specific response metric. PLoS ONE 8(1):1–7
127. Nia H, Datta M, Seano G, Zhang S, Ho W, Roberge S, Huang P (2020) In vivo compression and imaging in mouse brain to measure the effects of solid stress. Nat Protoc 15(8):2321–2340
128. Nia H et al (2017) Solid stress and elastic energy as measures of tumour mechanopathology. Nat Biomed Eng 1:0004
129. Ogden R, Hill R (1972) Large deformation isotropic elasticity: on the correlation of theory and experiment for incompressible rubberlike solids. Proc R Soc A 326(1567):565–584
130. Onwudiwe K, Najera J, Siri S, Datta M (2022) Do tumor mechanical stresses promote cancer immune escape? Cells 11(23):3840
131. Padhani A, Ollivier L (2001) The RECIST criteria: implications for diagnostic radiologists. Br J Radiol 74:983–986
132. Painter K, Hillen T (2013) Mathematical modelling of glioma growth: the use of Diffusion Tensor Imaging (DTI) data to predict the anisotropic pathways of cancer invasion. J Theor Biol 323:25–39

133. Pasternak O, Sochen N, Gur Y, Intrator N, Assaf Y (2009) Free water elimination and mapping from diffusion MRI. Magn Reson Med 62(3):717–730
134. Powathil G, Kohandel M, Sivaloganathan S, Oza A, Milosevic M (2007) Mathematical modeling of brain tumors: effects of radiotherapy and chemotherapy. Phys Med Biol 52(11):3291–3306
135. Prevost T, Balakrishnan A, Suresh S, Socrate S (2011) Biomechanics of brain tissue. Acta Biomater 7(1):83–95
136. Rajagopal K (1995) Multiple configurations in continuum mechanics. Rep Inst Comput Appl Mech 6
137. Rajagopal K, Tao L (1995) Mechanics of mixtures. World Scientific
138. Rockne R, Rockhill J, Mrugala M, Spence A, Kalet I, Hendrickson K, Lai A, Cloughesy T, Alvord E Jr, Swanson K (2010) Predicting the efficacy of radiotherapy in individual glioblastoma patients in vivo: a mathematical modeling approach. Phys Med Biol 55:3271–85
139. Rockne R, Alvord E Jr, Rockhill J, Swanson K (2009) A mathematical model for brain tumor response to radiation therapy. J Math Biol 58:561–578
140. Rockne RC et al (2015) A patient-specific computational model of hypoxia-modulated radiation resistance in glioblastoma using 18F-FMISO-PET. J R Soc Interface 12(103):20141174
141. Roos W, Batista L, Naumann S, Wick W, Weller M, Menck C, Kaina B (2007) Apoptosis in malignant glioma cells triggered by the temozolomide-induced DNA lesion O6-methylguanine. Oncogene 26(2):186–197
142. Seano G et al (2019) Solid stress in brain tumours causes neuronal loss and neurological dysfunction and can be reversed by lithium. Nat Biomed Eng 3:230–245
143. Sinclair G, Benmakhlouf H, Martin H, Brigui M, Maeurer M, Dodoo E (2018) The role of radiosurgery in the acute management of fourth ventricle compression due to brain metastases. Surg Neurol Int 9:112
144. Sivaloganathan S, Statsna M, Tenti G, Drake J (2005) Biomechanics of the brain: a theoretical and numerical study of Biot's equations of consolidation theory with deformation-dependent permeability. Int J Non-Linear Mech 40:1149–1159
145. Sneed ED, Folk RL (1958) Pebbles in the lower Colorado river, Texas a study in particle morphogenesis. J Geol 66(2):114–150
146. Sobey I, Wirth B (2006) Effect of non-linear permeability in a spherically symmetric model of hydrocephalus. Math Med Biol 23:339–361
147. Steed T, Treiber J, Brandel M, Patel K, Dale A, Carter B, Chen C (2018) Quantification of glioblastoma mass effect by lateral ventricle displacement. Sci Rep 8:2827
148. Stensjøen A, Solheim O, Kvistad K, Håberg A, Salvesen Ø, Berntsen E (2015) Growth dynamics of untreated glioblastomas in vivo. Neuro Oncol 17:1402–1411
149. Stewart DC, Rubiano A, Dyson K, Simmons CS (2017) Mechanical characterization of human brain tumors from patients and comparison to potential surgical phantoms. PLoS ONE 12:1–19
150. Stupp R et al (2009) Effects of radiotherapy with concomitant and adjuvant temozolomide versus radiotherapy alone on survival in glioblastoma in a randomised phase III study: 5-year analysis of the EORTC-NCIC trial. Lancet Oncol 10(5):459–466
151. Stupp R et al (2005) Radiotherapy plus concomitant and adjuvant temozolomide for glioblastoma. N Engl J Med 352(10):987–996
152. Stylianopoulos T, Martin J, Snuderl M, Mperkis F, Jain S, Jain R (2013) Coevolution of solid stress and interstitial fluid pressure in tumors during progression: implications for vascular collapse. Can Res 73:3833–3841
153. Stylianopoulos T et al (2012) Causes, consequences, and remedies for growth-inducedsolid stress in murine and human tumors. PNAS 109(38):15101–15108
154. Subramanian S, Gholami A, Biros G (2019) Simulation of glioblastoma growth using a 3D multispecies tumor model with mass effect. J Math Biol 79:941–967
155. Sunderland GJ, Jenkinson MD, Zakaria R (2016) Surgical management of posterior fossa metastases. J Neurooncol 130:535–542
156. Suveges S, Hossain-Ibrahim K, Steele J, Douglas RE, Trucu D (2021) Mathematical modelling of glioblastomas invasion within the brain: a 3D multi-scale moving-boundary approach. Mathematics 9:2214
157. Svensson S et al (2021) Decreased tissue stiffness in glioblastoma by MR Elastography is associated with increased cerebral blood flow. Eur J Radiol 147:110136
158. Swan A, Hillen T, Bowman J, Murtha A (2017) A patient-specific anisotropic diffusion model for brain tumour spread. Bull Math Biol 80:1259–1291
159. Swanson K, Alvord E Jr, Murray J (2000) A quantitative model for differential motility of gliomas in grey and white matter. Cell Prolif 33:317–29
160. Swanson K, Alvord E Jr, Murray J (2002) Quantifying efficacy of chemotherapy of brain tumors with homogeneous and heterogeneous drug delivery. Acta Biotheor 50:223–37
161. Swanson K, Alvord E Jr, Murray J (2002) Virtual brain tumours (gliomas) enhance the reality of medical imaging and highlight inadequacies of current therapy. Br J Cancer 86:14–8
162. Swanson K, Bridge C, Murray J, Alvord E Jr (2004) Virtual and real brain tumors: using mathematical modeling to quantify glioma growth and invasion. J Neurol Sci 216:1–10
163. Tanaka M, Debinski W, Puri I (2009) Hybrid mathematical model of glioma progression. Cell Prolif 42:637–46
164. TetGen. https://wias-berlin.de/software/tetgen/
165. The Vascular Modeling Toolkit. 2017. https://www.vmtk.org/
166. Tracqui P, Cruywagen G, Woodward D, Bartoo G, Murray J, Alvord E Jr (1995) A mathematical model of glioma growth: the effect of chemotherapy on spatio-temporal growth. Cell Prolif 28(1):17–31
167. Tysnes B, Mahesparan R (2001) Biological mechanisms of glioma invasion and potential therapeutic targets. J Neurooncol 53(2):129–147
168. Vidotto M, Bernardini A, Trovatelli M, De Momi E, Dini D (2021) On the microstructural origin of brain white matterhydraulic permeability. PNAS 118(36):e2105328118
169. Vidotto M, Botnariuc D, De Momi E, Dini D (2019) A computational fuid dynamics approach to determine white matter permeability. Biomech Model Mechanobiol 18:1111–1122
170. Wang C et al (2009) Prognostic significance of growth kinetics in newly diagnosed glioblastomas revealed by combining serial imaging with a novel biomathematical model. Can Res 69:9133–9140
171. Wang J, Huang Z, Lo S, Yuh W, Mayr N (2010) A generalized linear-quadratic model for radiosurgery, stereotactic body radiation therapy, and high dose rate brachytherapy. Sci Transl Med 2(39):39ra48
172. Wang X, June R, Pierce D (2021) A 3-D constitutive model for finite element analyses of agarose with a range of gel concentrations. J Mech Behav Biomed Mater 114:104150
173. Woodward D, Cook J, Tracqui P, Cruywagen G, Murray J, Alvord E Jr (1996) A mathematical model of glioma growth: the effect of extent of surgical resection. Cell Prolif 29(6):269–288
174. Woodward G, Dunn G, Nance E, Hanes J, Brem H (2014) Emerging insights into barriers to effective brain tumor therapeutics. Front Oncol 4:126
175. Xiao K, Ho S, Hassanien AE (2007) Brain magnetic resonance image lateral ventricles deformation analysis and tumor prediction. Malaysian J Comput Sci 20:115–32

176. Zhan W, Rodrigues y Baena F, Dini D, (2019) Effect of tissue permeability and drug diffusion anisotropy on convection-enhanced delivery. Drug Deliv 26(1):773–781